Centro de Investigación Científica y de Educación Superior de Ensenada, Baja California

Doctorado en Ciencias en Óptica con orientación en Óptica Física

---

Compact dual wavelength sources based on aperiodically poled lithium niobate and their use in obtaining tunable narrowband terahertz radiation.

Tesis

para cubrir parcialmente los requisitos necesarios para obtener el grado de

Doctor en Ciencias

Presenta:

Miriam Patricia Carrillo Fuentes

Ensenada, Baja California, México

2020

Tesis defendida por

Miriam Patricia Carrillo Fuentes

y aprobada por el siguiente Comité

Dr. Roger Sean Cudney Bueno
Director de tesis

Dra. Mojca Jazbinsek

Dr. Santiago Camacho López

Dr. Anatoly Khomenko

Dr. Israel Rocha Mendoza
Coordinador del Posgrado en Óptica

Dra. Rufina Hernández Martínez
Directora de Estudios de Posgrado

Miriam Patricia Carrillo Fuentes © 2020

Queda prohibida la reproducción parcial o total de esta obra sin el permiso formal y explícito del autor y director de la tesis

Resumen de la tesis que presenta Miriam Patricia Carrillo Fuentes como requisito parcial para la obtención del grado de Doctor en Ciencias en Óptica con orientación en Óptica Física.

Fuentes duales compactas basadas en niobato de litio aperiódicamente polarizado y su uso para obtener radiación terahertz sintonizable con ancho de banda angosto.

Resumen aprobado por:

Dr. Roger Sean Cudney Bueno
Director de tesis

En este trabajo se reporta el desarrollo de un par de fuentes pulsadas basadas en oscilación óptica paramétrica (OPO) y en generación óptica paramétrica (OPG) usando como medio de ganancia un cristal de niobato de litio aperiódicamente polarizado (APLN). El objetivo principal de estas fuentes es usarlas como fuente de bombeo para obtener radiación de terahertz por resta de frecuencias usando como medio nolineal el cristal orgánico HMQ-TMS. El cristal APLN fue diseñado para generar dos señales con sus correspondientes acompañantes a partir de un solo pulso de bombeo; la longitud de onda de las señales está centrada alrededor de 1450 nm, y la diferencia de frecuencia entre ellas se puede sintonizar entre ∼ 1 y 10 THz. En la configuración OPO, se usó como fuente de bombeo un láser pulsado de Nd:YAG (12 ns FWHM, y un máximo de energía por pulso de 13 mJ), obteniendo un par de señales sincronizadas (∼ 5 ns FWHM) con una energía combinada de 740 μJ; cada señal tiene un ancho de banda de <105 GHz. En la configuración OPG utilizamos un láser pulsado Nd:YLF que emite pulsos más cortos (1.6 ns FWHM, 350 *mu* J), obteniendo pulsos de señal sincronizados con una energía combinada de 38 μ J; cada señal tiene un ancho de pulso de 0.8 ns y un ancho de banda <175 GHz. Presentamos también la generación de THz por resta de frecuencias (DFG) usando el cristal HMQ-TMS. Con el sistema OPO obtuvimos un máximo de 47 nJ para 1.21 THz con una energía combinada de señales de 740 μJ, con una eficiencia máxima del 0.0062%. Usando el sistema basado en OPG obtuvimos un máximo de 40 nJ para 2.39 THz, con una energía combinada de las señales de 35 μJ, con una eficiencia máxima del 0.1 %.

Palabras clave: láseres, óptica nolineal, niobato de litio, generación de THz

Abstract of the thesis presented by Miriam Patricia Carrillo Fuentes as a partial requirement to obtain the Doctor of Science degree in Name of the Degree with orientation in physical optics.

Compact dual wavelength sources based on aperiodically poled lithium niobate and their use in obtaining tunable narrowband terahertz radiation.

Abstract approved by:

Dr. Roger Sean Cudney Bueno
Thesis Director

The objective of this thesis is to develop two sources of synchronized pairs of pulses based on optical parametric generation (OPG) and oscillation (OPO) that use aperiodically poled lithium niobate (APLN) as the nonlinear medium. The main purpose of these sources is to obtain terahertz radiation through difference-frequency generation. The APLN crystal was designed to generate two signals with their corresponding idlers from a single pump pulse; the signal wavelengths are around 1450 nm, and the frequency difference between them is tunable between ∼1 and 10 THz. In the OPO configuration, pumped by a Q-switched Nd:YAG laser (12 ns FWHM, 13 mJ), we obtain pairs of synchronized signals (∼ 5 ns FWHM) with a combined energy of 740 μJ; each signal has a bandwidth of <105 GHz. In the OPG configuration, we use a Q-switched Nd:YLF laser that emits shorter pulses (1.6 ns FWHM, 350 μJ), obtaining synchronized signal pulses with a combined energy of 38 μJ; each signal has a pulse width of 0.8 ns and a bandwidth of <175 GHz. The advantages of these sources for difference frequency generation are discussed. Both configurations OPO and OPG were used to obtain terahertz radiation that can be tuned to well-defined frequencies spanning ∼ 1.2 to 10 THz, based on difference-frequency generation in an HMQ-TMS crystal. In OPO configuration we obtain maximum of 47 nJ for 1.21 THz using 740 μJ, 5 ns pulses while using OPG configuration the maximum that we obtained was 40 nJ for 2.39 THz THz pulses using 38 μJ, 0.85 ns pump pulses.

Keywords: lasers, nonlinear optics, niobato de litio, THz generation

Dedicatoria

Com amor a mis padres, Lucio Carrillo y Josefina Fuentes.

A la memoria de mi querido amigo Ketzasmín Terrón.

Agradecimientos

A la naturaleza, por su eterno encanto.

A mi asesor, Dr. Roger Cudney, por todos estos años de paciencia y enseñanza. Por permitirme ser parte de este barco que navega en las olas de la nolinealidad. Por enseñarme tanto cada día y por brindarme su amistad y confianza.

A mi comité de tesis, Dr. Santiago Camacho, Dr. Anatoly Komenko y Dra. Mojca Jazbinsek, por el tiempo invertido en mi trabajo, por su paciencia y sobre todo porque cada presentación era un motivo para ser mejor. Thanks Dra. Mojca for the organic crystal that allows us to obtain THz radiation.

A Luis Ríos, por la ayuda técnica que me salvó más de una vez pero, sobre todo, por la amistad y el tiempo compartido, siempre te estaré agradecida.

La vida en la Baja no sería igual sin mis amigos Israel Gómez y Joanna Vargas, por todos estos años, por su apoyo, amistad, por estar presentes y por el cariño ¡un millón de gracias!

A mis compañeros de *El cubo de los lamentos*: Anna, Avril, Lili, Carlos y Germán, por el drama y las risas compartidas, por hacer del cubo un sitio especial. Gracias también a Alma González por su amistad y apoyo incondicional.

A todo el personal de Física Aplicada quienes hacen de este un lugar muy grato. Especialmente a Carmen Ochoa por todo el apoyo brindado en este tiempo, por las alegrías y su paciencia y a Isaac Fimbres por toda su ayuda con las peripecias computacionales.

A mis padres Lucio Carrillo y Josefina Fuentes por la vida, el amor, los viajes y todo lo que su inmenso corazón me da. A mi hermana Ana Carrillo y a su hermosa familia

Ulises Bautista y mi adorada Vale, por sus abrazos cariñosos y generosos, el amor que me dan siempre será correspondido.

A José Luis Bueno por la amistad, el tiempo, el mar, la comida, la cerveza y las risas compartidas. Siempre tendrás un lugar especial en mi corazón.

A la sociedad mexicana que, a través del Consejo Nacional de Ciencia y Tecnología (CONACyT), me brindó el apoyo económico para realizar mis estudios de doctorado. No. de becario: 275874

Al CICESE por haberme brindado la oportunidad de realizar mis estudios de posgrado. A Dolores Sarracino por su comprensión y apoyo en tiempos oscuros. Al Dr. Israel Rocha por su apoyo.

A Ensenada. Te voy a extrañar.

A Grupo Molecular por su apoyo en este último sprint.

Que lo que aquí escribí se lo lleve el mar.

Table of contents

Page

Table of contents

List of figures

List of figures

List of figures

List of figures

List of tables

Chapter 1. Introduction

Coherent light sources based on nonlinear optical materials enable a wide variety of photonic applications. Soon after the second harmonic generation of a ruby laser pulse using quartz as a nonlinear medium was demonstrated in 1961 by Franken et. al., other nonlinear processes such as optical parametric processes enabled devices that provide a widely tunable radiation. It was in 1965 when Giordmaine and Miller built the first tunable optical parametric oscillator based on lithium niobate (Giordmaine and Miller, 1965). In this experiment, the emission generated was in the wavelength range of 0.97 to 1.15 μm, with optical pumping at 529 nm. The optical parametric oscillator (OPO) consisted of a nonlinear crystal within a resonator formed by a pair of mirrors. The nonlinear interactions that give rise to the creation of a pair of the output wavelengths are known as optical parametric generation, optical parametric amplification and optical parametric oscillation.

In optical parametric generation (OPG), a wave of frequency ω_p coming from a laser interacts with a medium with a second order nonlinear crystal $\chi^{(2)}$. The nonlinear interaction causes the generation of two new waves, known as *signal* and *idler* waves of frequencies ω_s and ω_i. From a quantum point of view, the nonlinear medium annihilates a pump photon and creates a signal and an idler photon. Energy and momentum conservation rules must be simultaneously satisfied, which implies that:

$$\hbar\omega_p = \hbar\omega_s + \hbar\omega_i, \tag{1}$$

and

$$\hbar\mathbf{k}_p = \hbar\mathbf{k}_s + \hbar\mathbf{k}_i, \tag{2}$$

where $\hbar$ is Planck's constant and $\hbar\mathbf{k}_p$, $\hbar\mathbf{k}_s$ and $\hbar\mathbf{k}_i$ are the photon momentum of the pump, signal an idler waves. When $\Delta\mathbf{k} = \mathbf{k}_p - \mathbf{k}_s - \mathbf{k}_i = 0$, it is said that the phase matching condition is satisfied. The magnitude of the wavevector is given by the dispersion relation $|\mathbf{k}| = \omega n/c$, where n is the refractive index and c is the speed of light in vacuum. If the propagation of the beams is collinear in the medium, then Eq. 2 can be written as

$$\frac{n_p}{\lambda_p} = \frac{n_s}{\lambda_s} + \frac{n_i}{\lambda_i}, \tag{3}$$

where λ_p, λ_s, and λ_i are the pump, signal and idler wavelengths, respectively.

The process of optical parametric generation is illustrated in Fig. (1 a). Once the signal and idler waves are generated they can continue to interact with the pump beam; the signal and idler are amplified while the pump is depleted. This process is known as optical parametric amplification (OPA), shown in Fig. (1 b), where the seed is the signal but it could be the idler. If the nonlinear medium is placed inside a cavity resonator then the mirrors feed back the waves into the nonlinear medium and the amplification process continues. Above the threshold for oscillation, that is, when the gain produced by OPA is larger than the losses introduced by the cavity, the signal and idler waves grow dramatically. A schematic OPO is shown in Fig. (1 c).

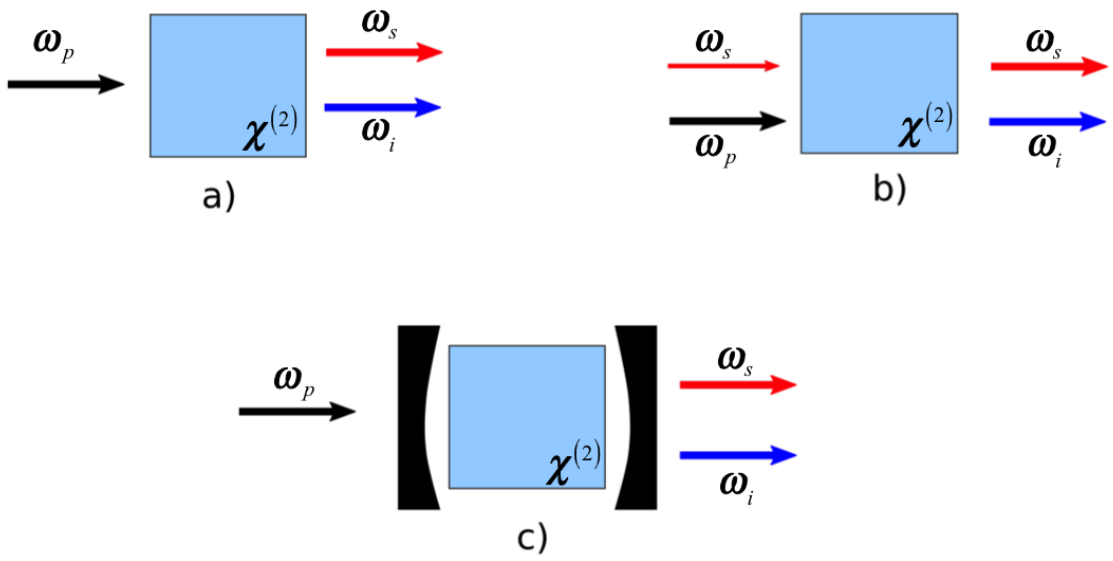

Figure 1. Parametric processes: a) optical parametric generation; b) optical parametric amplification and c) optical parametric oscillation

The signal and idler frequencies are determined by Eq. 1 and Eq. 3. Since the refractive index depends on the wavelength (dispersion), it is not possible to satisfy both of these equations simultaneously in isotropic media; it is necessary to use anisotropic nonlinear materials, such as birefringent crystals, where the refractive indexes depend on the direction of propagation and the polarization of the waves. By using waves with different polarizations, phase-matching can be achieved in these materials.

From a wave propagation point of view, phase-matching is nothing more than the requirement that all the signal waves generated throughout the medium are in phase with each other; the same applies to the idler waves. That is the reason why this technique is called “phase-matching”. Otherwise, if the waves generated throughout

the medium are not in phase there can be destructive interference among them, which limits the total intensity of the resulting wave, as shown in Fig. (2 a). Dispersion causes the waves to propagate at different velocities throughout the medium; it is this velocity mismatch that causes the generated waves to get out of phase. The length of the medium in which all of the generated signal waves interfere constructively (maximum phase difference of 180°) is called the coherence length and is given by $l_c = \frac{\pi}{|\Delta k|}$. Typically, for isotropic media the coherence length in the optical range is of the order of a few microns. For different reasons which will become apparent later on, phase-matching is not used in the work described in this thesis; instead we use quasi-phase-matching (QPM).

Quasi phase matching consists in adding a 180° phase shift to the generated waves every coherence length l_c (Armstrong *et al.*, 1962). This can be achieved by using nonlinear materials where the second order susceptibility $\chi^{(2)}$ switches its sign each coherence length, as shown in Fig. (2 b). Let $\Lambda = 2l_c$ be the switching period; then the quasi-phase-matching condition is given by:

$$\left| \frac{n_p}{\lambda_p} - \frac{n_s}{\lambda_s} - \frac{n_i}{\lambda_i} \right| = \frac{1}{\Lambda}. \tag{4}$$

From this equation it is seen that the period determines the generated signal and idler wavelengths.

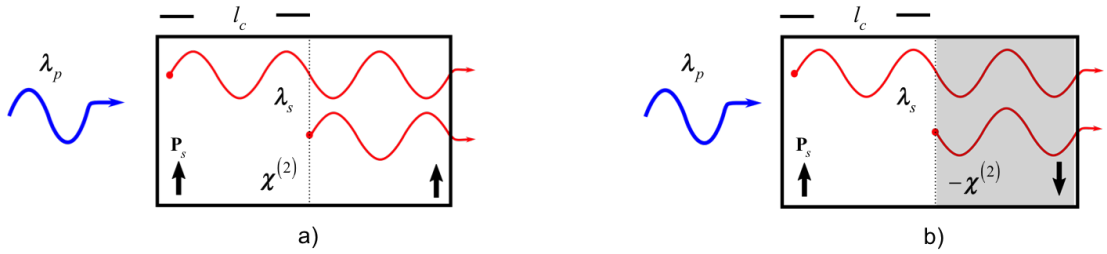

Figure 2. Phase mismatch. In a) the generated signal waves are mismatched; in (b) the sign of the nonlinearity is flipped and the generated signal waves are in phase and there is constructive interference.

The most common way to implement QPM is by using ferroelectric crystals such as lithium niobate ($LiNbO_3$), lithium tantalate ($LiTaO_3$) and potassium titanyl phosphate (KTP, $KTiOPO_4$). In this work we only use lithium niobate crystals. Ferroelectric materials have an intrinsic dipole moment known as the spontaneous polarization $\mathbf{P}_s$, which can be switched when a strong electric field is applied for some time. The magnitude of the electric field required to flip the direction of the spontaneous polarization is known

as the coercive field. Once $\mathbf{P}_s$ is flipped it remains in the new direction when the electric field is removed. Figure (3) shows that by periodically flipping the direction of the spontaneous polarization a periodic ferroelectric domain structure is created. Periodic electrodes are placed on one of the surfaces of the ferroelectric material and a high voltage is applied to them; the direction of the polarization is flipped underneath the electrodes while the rest of the medium is left intact. Detailed physical characteristics about lithium niobate are given in Chapter (3).

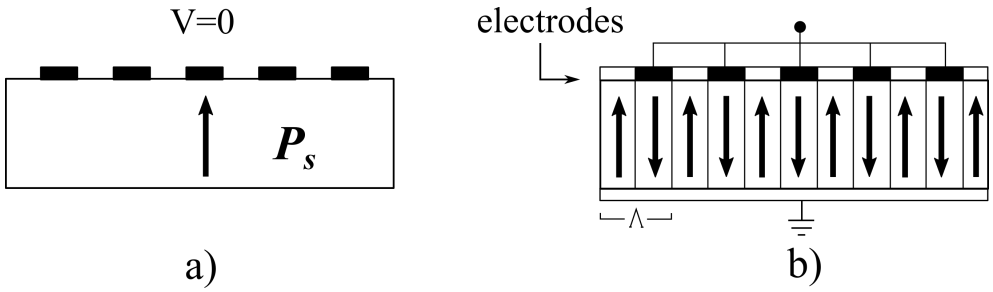

Figure 3. When no voltage is applied in the lithium niobate wafer as in (a) we have a ferroelectric mono-domain and, (b) when a high voltage is applied through the electrodes, the direction of the spontaneous polarization is flipped.

It is common to design a crystal with two or more periods, as shown in Fig. (4 a) so that each section of the crystal will generate a different signal with its corresponding idler. Another design is the aperiodically poled lithium niobate (APLN) and consists in scrambling both periods throughout all the crystal, as illustrated in Fig. (4 b). The main advantage of the APLN design over the periodic one is that, since both nonlinear interactions take place all over the crystal length, the conversion to the desired signal and idler wavelengths is more efficient and the bandwidths of the generated signals are narrower (Robles-Agudo and Cudney, 2011). This topic will be discussed in more detail in the next chapters.

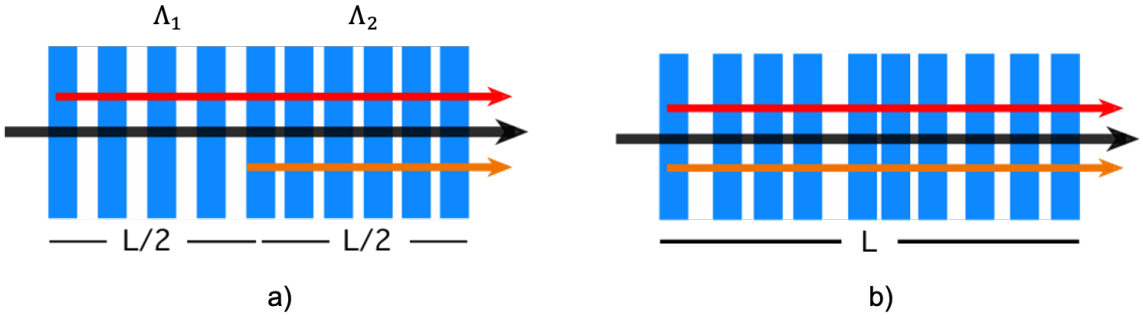

Figure 4. Two different designs to generate two different nonlinear processes: a) two separate periodic structures and, b) an aperiodic structure.

In this thesis an aperiodically poled lithium niobate design is developed to build a tunable dual-wavelength source. The emission is centered around ∼ 1450 nm and the pair of signals generated has a tunable difference in frequency of ∼ 1-10 THz. The emission will be mixed in an organic nonlinear crystal (HMQ-TMS) to generate tunable THz radiation. The APLN crystal is used in two configurations: one consists of an optical parametric oscillator (OPO) and the other one is based on optical parametric generation (OPG), as are illustrated in Fig. (5). In the OPO configuration we use as the pump source a Q-switched Nd:YAG laser (λ = 1064 nm) with pulses of 10 ns (FWHM), the energy per pulse is in the 1-10 mJ range at a 5 Hz repetition rate. In the OPG configuration we use a Q-switched Nd:YLF laser (λ= 1047 nm), built in our laboratory, that emits shorter pulses (1.5-1.6 ns, FWHM) at a repetition rate of 27 Hz. This laser was built based on the design described in (Cudney and Minor, 2018). In both experimental configurations both signals are synchronized and spatially overlapped. The output emission is filtered to remove the remnant pump beam and idler beams, and the signals are mixed in a nonlinear organic crystal (HMQ-TMS), producing terahertz radiation by difference-frequency generation (DFG); this terahertz radiation is detected by a pyroelectric detector. Both configurations are a compact dual wavelength system; all the experimental details are given in next chapters.

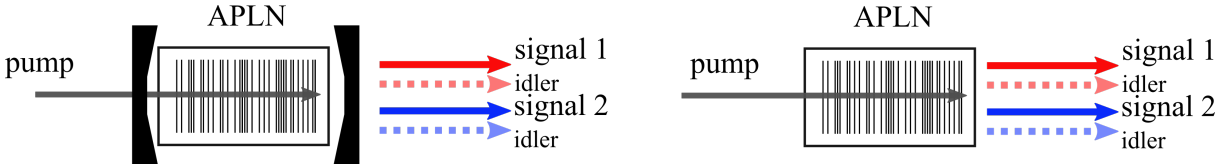

Figure 5. Optical parametric oscillator and optical parametric generation. Experiments were performed using both configurations in order to compare the emission generated using the same APLN sample.

Terahertz radiation is a region in the electromagnetic spectrum that is located between microwaves and infrared light; roughly speaking, in terms of frequency it corresponds to ∼ 0.1 - 10 THz, (see Fig (6)). This kind of radiation is of great interest for different applications in many fields: from astronomy, since the universe is bathed in terahertz radiation from the Big Bang (Dole *et al.*, 2006), to medicine, where THz imaging and forensic science are very promising applications (Dhillon *et al.*, 2017) and, even in the art field where pulsed THz sources are used in non-invasive technique to analyze paintings (Abraham *et al.*, 2010).

The generation of terahertz radiation by difference frequency generation requires

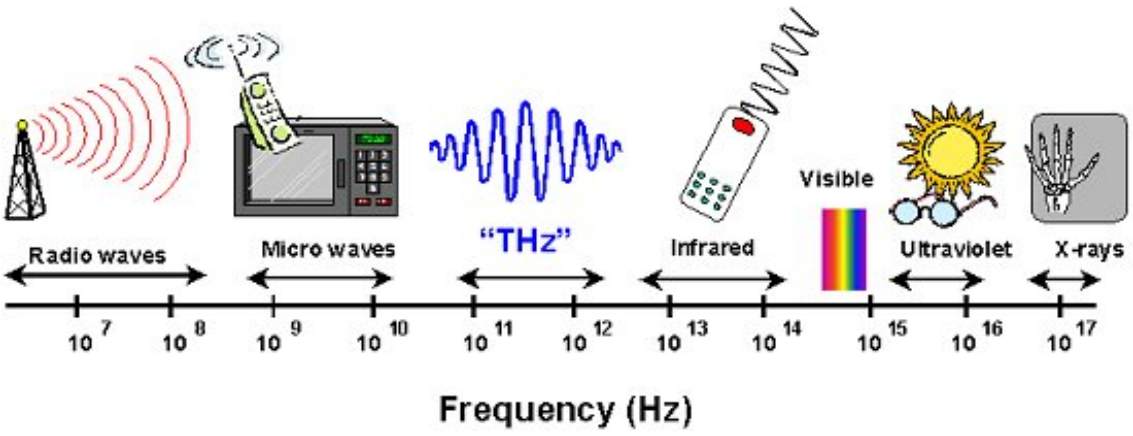

Figure 6. Electromagnetic spectrum (Image from web Institut für planetensforschung)

the interaction of two narrowband beams of similar but slightly different frequencies ω_1 and ω_2 in a nonlinear medium, such that their frequency difference lies in the terahertz range. Organic crystals such as OH1, DAST, DSTMS, BNA and HMQ-TMS are specially designed with a high second order nonlinearity and have been used to generate THz radiation not only by DFG but by other means. The most common is by optical rectification (OR) where a broadband femtosecond pulse is used to create a broadband terahertz pulse. It was first demonstrated in DAST using a 150 fs pulse centered at 820 nm as the pump (Zhang *et al.*, 1992). It is also possible to obtain THz radiation using inorganic crystals such as lithium niobate, ZnTe, GaP, GaAs, GaSe; however the high absorption in THz limits its efficiency (Kitaeva, 2008).

The production of THz by difference frequency generation (DFG) has been reported by several groups where the pair of frequencies come from a pulsed OPO based on PPLN and are mixed in an organic DAST crystal (Kawase *et al.*, 2000), (Taniuchi *et al.*, 2004), or in a GaP crystal (Taniuchi and Nakanishi, 2004), and a comparison between PPLN and APLN in (Lhuillier *et al.*, 2007). In the OPO configuration used by Kawase and Ito (Kawase *et al.*, 2000), both signals are generated from a single 40 mm long PPLN sample that has two sections, each with a different period. The experimental setup is shown in Fig. (7). From this configuration they obtained a THz-wavelength tuning from 100 to 700 μm, which in frequency corresponds to 0.5-3 THz. The tuning was achieved by producing various periods in the crystal sample.

The main advantages of generating both wavelengths from a parametric process (OPO or OPG) is that the source is compact and the signals are generated synchronously.

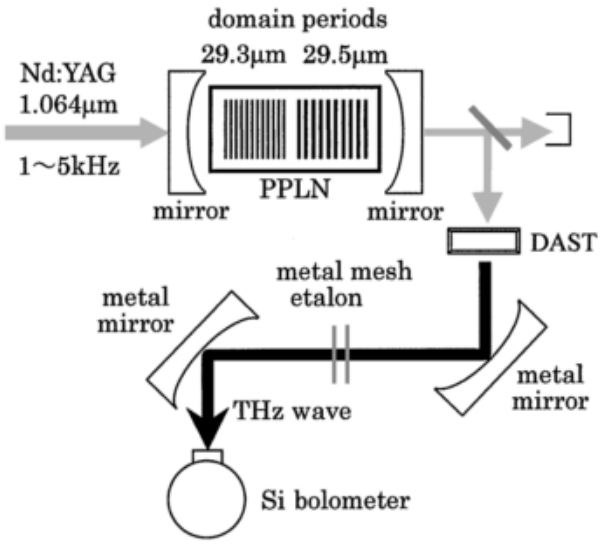

Figure 7. Experimental set up in (Kawase *et al.*, 2000) for THz generation by DFG in the organic crystal DAST.

There are other ways to generate THz using two independent solid-state lasers and the THz radiation comes from semiconductor nonlinear crystals such as zinc telluride (ZnTe), gallium phosphide (GaP) or gallium selenide (GaSe). In Fig. (8), two Nd:YLF crystals generate two beams, one at 1047 nm and the other at 1053 nm. Since the 1047 nm and 1053 nm beams have perpendicular polarization directions, the two laser crystals were placed at two divided arms decoupled by a polarizer. An acousto optic Q-switch was placed at the shared arm of the two laser cavities. Thus, the dual-frequency pulses are synchronized by simultaneously modulating the losses of the two cavities (Ding, 2014).

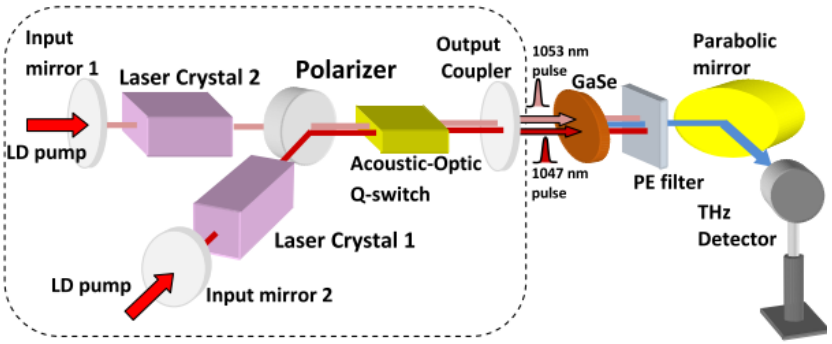

Figure 8. THz generation by DFG in a GaSe crystal using two solid state lasers.

There are many ways to generate THz radiation and the design, fabrication and THz sources still is a challenge. This thesis presents a compact, tunable and efficient THz source and experimentally easy to handle. The organization of this manuscript is

described below.

1.1 Organization of the thesis

In Chapter 2 the nonlinear theory that rules over parametric generation and oscillation is presented from a general point of view. The generation of the two signals using an aperiodical poled crystal is described by the theory of quasi-phase matching, described in this Chapter.

Lithium niobate is the crystal used in this work, therefore, its optical properties are described in Chapter 3. The experimental technique to create the aperiodic structure in the crystal is also described.

The description of the DFG for THz generation is given in Chapter 5. The optical properties of the organic nonlinear crystal used are presented. The THz detection system is also described.

In Chapter 5 all the experimental set ups are described. The results obtained for THz pulses using the designed APLN crystal in the OPO configuration and the OPG configuration are presented.

In Chapter 6 conclusions of the work developed in this thesis are presented. In this last chapter there is a comparison between the two experiments designed to generate THz radiation.

Chapter 2. Theory of nonlinear processes

Nonlinear effects are a consequence of the interaction of a high intensity electromagnetic field with a material; this interaction modifies its optical properties. In this Chapter, the theory that describes the optical parametric generation and oscillation is presented.

2.1 Nonlinear interaction of radiation and matter

According to the Lorentz model, each atom in a dielectric material is considered as an oscillating dipole joined by a spring as shown in Fig. (9 a). If an external electromagnetic field, $E(t) = E_0 e^{-i\omega t}$, interacts with this material, the distance between the electron and the nucleus changes, as shown in Fig. (9 b). This displacement causes a dipole moment that contributes to the polarization and electric susceptibility of the dielectric medium.

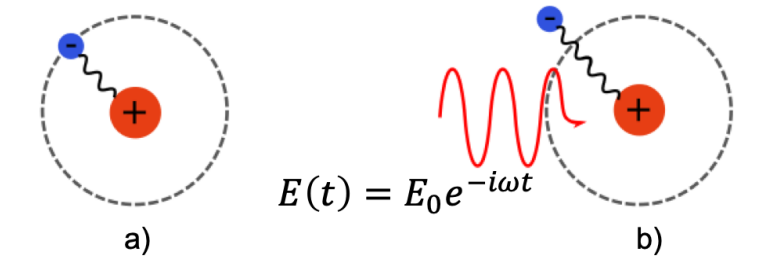

Figure 9. Lorentz model a) atom seen as a dipole held together with a spring; b) Interaction of light with the dipole.

The oscillating charges in the material are described by a polarization term, **P**, that corresponds to the sum of the atomic dipole moments per unit volume. For low intensity fields, the displacement depends linearly on the external field and the oscillations generated follow the incident wave, giving as a result waves of radiation of the same frequency as the incident field; however, if the intensity of the electric fields is higher the polarization response of the medium becomes nonlinear and the displacement of the electrons is distorted. This distortion causes the generation of waves with frequencies that are not the same as the frequency of the incident electric field.

In the linear case and, considering a local dependence, the polarization is given by:

$$\mathbf{P}(\mathbf{r},t)=\int_{-\infty}^{\infty}\overline{\overline{\chi}}^{(1)}\left(\mathbf{r}',t-t'\right)\cdot\mathbf{E}(\mathbf{r}',t')dt', \tag{5}$$

where $\overline{\overline{\chi}}^{(1)}$ is the linear susceptibility tensor. Considering a unidimensional case in which $\mathbf{E}$ is a plane monochromatic wave given by $\mathbf{E}(x,t)=\frac{1}{2}\sum_j\hat{\mathbf{e}}_jE_je^{i(k_jx-\omega t)}+c.c.$, then Eq. 5 is expressed as

$$\mathbf{P}(\mathbf{r},t)=\frac{1}{2}\epsilon_0\sum_jE_je^{ik_jx}\int_{-\infty}^{t}\overline{\overline{\chi}}^{(1)}\left(\mathbf{r}',t-t'\right)\cdot\hat{\mathbf{e}}_je^{-i\omega_jt'}dt'+c.c. \tag{6}$$

The Fourier transform of $\overline{\overline{\chi}}$ is defined as:

$$\overline{\overline{\chi}}(\mathbf{r},t)=\frac{1}{\sqrt{2\pi}}\int_{-\infty}^{\infty}\overline{\overline{\chi}}^{(1)}(\mathbf{r},\omega)e^{-i\omega t}d\omega\quad\text{and}\quad\overline{\overline{\chi}}(\mathbf{r},\omega)=\frac{1}{\sqrt{2\pi}}\int_{-\infty}^{\infty}\overline{\overline{\chi}}^{(1)}(\mathbf{r},t)e^{i\omega t}dt. \tag{7}$$

Considering this, Eq. 6 is expressed as

$$\begin{aligned}\mathbf{P}(\mathbf{r},t)&=\frac{1}{2}\epsilon_0\sum_jE_je^{ik_jx}\frac{1}{\sqrt{2\pi}}\int_{-\infty}^{\infty}\int_{-\infty}^{t}\overline{\overline{\chi}}^{(1)}\left(\mathbf{r}',\omega\right)e^{-i\omega(t-t')}\cdot\hat{\mathbf{e}}_je^{-i\omega_jt'}dt'd\omega+c.c.\\&=\frac{1}{2}\epsilon_0\sum_jE_je^{ik_jx}\frac{1}{\sqrt{2\pi}}\int_{-\infty}^{\infty}\overline{\overline{\chi}}_t^{(1)}\left(\mathbf{r}',\omega\right)e^{-i\omega t}\cdot\hat{\mathbf{e}}\underbrace{\left[\int_{-\infty}^{\infty}e^{it'(\omega-\omega_j)}dt'\right]}_{\text{Dirac delta}}d\omega+c.c.,\end{aligned} \tag{8}$$

where

$$\overline{\overline{\chi}}_t(\mathbf{r},t-t')=\begin{cases}\chi(\mathbf{r},t-t') & \text{if } t-t'>0\\ 0 & \text{if } t-t'<0.\end{cases} \tag{9}$$

Then, using Eq. 6

$$\begin{aligned}\mathbf{P}(\mathbf{r},t)&=\frac{1}{2}\epsilon_0\sum_jE_je^{ik_jx}\sqrt{2\pi}\int_{-\infty}^{\infty}\overline{\overline{\chi}}^{(1)}\left(\mathbf{r}',\omega\right)\cdot\hat{\mathbf{e}}_je^{-i\omega t}\delta(\omega-\omega_j)d\omega+c.c.\\&=\frac{1}{2}\epsilon_0\sqrt{2\pi}\sum_jE_je^{i\left[k_jx-\omega_jt\right]}\overline{\overline{\chi}}^{(1)}(\mathbf{r},\omega)\cdot\hat{\mathbf{e}}_j+c.c.\end{aligned} \tag{10}$$

Finally, $\mathbf{P}(\mathbf{r},t)$ is expressed as:

$$\mathbf{P}(\mathbf{r},t)=\frac{1}{2}\sqrt{2\pi}\sum_m\hat{\mathbf{e}}_mP_me^{i(k_mx-\omega_mt)}+c.c., \tag{11}$$

where

$$P_m = P(\omega_m) = \epsilon_0 E_\omega \overline{\overline{\chi}}_t^{(1)}(\mathbf{r}, \omega_m). \tag{12}$$

Lasers provide a high intensity electromagnetic field, which give rise to nonlinear phenomena. The polarization is expanded as a power series as follows:

$$\begin{aligned}\mathbf{P}(\omega) = \epsilon_0 \Big[& \overline{\overline{\chi}}^{(1)}(\omega) \cdot \mathbf{E}(\omega) + \overline{\overline{\overline{\chi}}}^{(2)}(\omega; \omega_1, \omega_2) : \mathbf{E}(\omega_1)\mathbf{E}(\omega_2) \\ & + \overline{\overline{\overline{\chi}}}^{(3)}(\omega; \omega_1, \omega_2, \omega_3) : \mathbf{E}(\omega_1)\mathbf{E}(\omega_2)\mathbf{E}(\omega_3) + \ldots \Big]\end{aligned} \tag{13}$$

where ϵ_0 is the vacuum permittivity. The linear and nonlinear susceptibilities characterize the optical properties of a medium and they are related to the microscopic structure of the medium.

The polarization is given by $\mathbf{P} = \mathbf{P}_L + \mathbf{P}_{NL}$, where $\mathbf{P}_L$ is the part of the electric dipole linear polarization and, $\mathbf{P}_{NL}$ is the nonlinear part of this polarization. Linear polarization describes all the phenomena in the regime where the optical properties of a medium are independent of the field intensity. The study of phenomena that arise from second order nonlinearity $\chi^{(2)}$, such as optical parametric generation and oscillation, are the objective of this thesis.

2.2 Coupled equations

The equation that describes the propagation of light through a nonlinear optical medium is the wave equation. The wave equation is deduced from Maxwell's equations, which are:

$$\nabla \cdot \mathbf{D} = \rho, \tag{14}$$

$$\nabla \cdot \mathbf{B} = 0, \tag{15}$$

$$\nabla \times \mathbf{E} = -\mu_0 \frac{\partial \mathbf{H}}{\partial t}, \tag{16}$$

$$\nabla \times \mathbf{H} = \mathbf{J} + \frac{\partial \mathbf{D}}{\partial t}, \tag{17}$$

where $\mathbf{D} = \epsilon_0 \mathbf{E} + \mathbf{P}$ is the electric displacement field, and $\mathbf{H}$ is the magnetic field, given by $\mathbf{H} = 1/\mu_0(\mathbf{B} - \mathbf{M})$, where $\mathbf{B}$ is the magnetic flux and $\mathbf{M}$ is the magnetization.

From this set of equations, and assuming a nonconducting dielectric material we get

$$\nabla(\nabla\cdot\mathbf{E})-\nabla^2\mathbf{E}+\frac{1}{c^2}\frac{\partial^2\mathbf{E}}{\partial t^2}=\mu_0\frac{\partial^2\mathbf{P}}{\partial t^2} \tag{18}$$

If the interaction occurs in a nonlinear crystal and the electric field is parallel to one of the axes of the crystal, which is the case in this work, it can be shown that $\nabla\cdot\mathbf{E}=0$ and the wave equation is given by

$$\nabla^2\mathbf{E}-\frac{1}{c^2}\frac{\partial^2\mathbf{E}}{\partial t^2}=\mu_0\frac{\partial^2\mathbf{P}}{\partial t^2}. \tag{19}$$

This is the wave equation with the polarization $\mathbf{P}$ as a source. To solve Eq. 19, it is assumed that the electromagnetic field and the polarization are a set of three plane, monochromatic waves that propagate in the x direction given by:

$$\mathbf{E}(x,t)=\sum_l^3 E_l(x)exp(ik_l x-\omega_l t)\hat{\mathbf{e}}_l+c.c., \tag{20}$$

where, $E_l(x)$ is the field amplitude, $\hat{\mathbf{e}}_l$ is the polarization unitary vector and k_l is the magnitude of the wave vector. Considering this, the spatial derivatives in Eq. (19) are given by

$$\nabla^2\mathbf{E}=\sum_l\hat{\mathbf{e}}_l\left[\frac{d^2E_l}{dx^2}+2ik_l\frac{dE_l}{dx}-k_l^2E_l\right]e^{i(k_lx-\omega_lt)}+c.c. \tag{21}$$

The linear term of the polarization is given by

$$\begin{aligned}\mathbf{P}^{(1)}&=\sum_l\mathbf{P}^{(1)}(\mathbf{k}_l,\omega_l),\\&=\epsilon_0\sum_l^3\overline{\overline{\chi}}^{(1)}(\omega_l.\omega_l)\cdot\hat{\mathbf{e}}_lE_l(x)e^{ik_lx}e^{i(\omega_lt)}+c.c.,\end{aligned} \tag{22}$$

and the second order nonlinear polarization is

$$\begin{aligned}\mathbf{P}^{(2)}&=\sum_l\mathbf{P}^{(2)}(\mathbf{k}_l,\omega_l),\\&=\epsilon_0\sum_{l=1}\sum_{n,m}\overline{\overline{\chi}}^{(2)}(\omega_l;\omega_n,\omega_m):\hat{\mathbf{e}}_n\hat{\mathbf{e}}_mE_n(x)E_m(x)e^{i(\omega_lt)}e^{i(k_n+k_m)}+c.c.\end{aligned} \tag{23}$$

Considering that the amplitude of the field varies slowly along the x direction, an approximation known as *slowly varying envelope approximation* $\left(\frac{d^2E}{dx^2}\ll|k_l\frac{dE_l}{dx}|\ll|k_lE_l|\right)$

is used, therefore Eq. (21) can be written as

$$\nabla^2\mathbf{E} \approx \sum_{l=1}^{3}\hat{\mathbf{e}}_l\left[2ik_l\frac{dE_l}{dx} - k_l^2E_l\right]e^{i(k_lx-\omega_lt)}. \tag{24}$$

Now, for the temporal derivatives:

$$\begin{aligned}\frac{1}{c^2}\frac{d^2\mathbf{E}}{dt^2} + \mu_0\frac{d^2\mathbf{P}}{dt^2} =& \frac{1}{c^2}\Bigg[\frac{d^2}{dt^2}\sum_l E_l(x)e^{i(k_lx-\omega_lt)}\hat{\mathbf{e}}_l \\ &+ \frac{d^2}{dt^2}\sum_l\overline{\overline{\chi}}^{(1)}(\omega_l;\omega_l)E_l(x)e^{i(k_lx-\omega_lt)}\hat{\mathbf{e}}_l \\ &+ \frac{d^2}{dt^2}\sum_l\sum_n\sum_m\overline{\overline{\overline{\chi}}}^{(2)}(\omega_l;\omega_n,\omega_m):\hat{\mathbf{e}}_n\hat{\mathbf{e}}_mE_nE_me^{i(k_lx-\omega_lt)} + c.c.\Bigg] \\ =& -\sum_l\frac{\omega_l^2}{c^2}E_le^{i(k_lx-\omega_lt)}\hat{\mathbf{e}}_l - \sum_l\frac{\omega_l^2}{c^2}\overline{\overline{\overline{\chi}}}^{(2)}(\omega_l,\omega_l)\cdot\hat{\mathbf{e}}_lE_le^{i(k_lx-\omega_lt)} \\ &-\sum_l\sum_n\sum_m\frac{\omega_l^2}{c^2}\overline{\overline{\overline{\chi}}}^{(2)}(\omega_l;\omega_n,\omega_m):\hat{\mathbf{e}}_n\hat{\mathbf{e}}_mE_nE_me^{i(k_lx-\omega_lt)} + c.c.\end{aligned} \tag{25}$$

The terms oscillating at ω_l:

$$\begin{aligned}\sum_l\left[2ik_l\frac{dE_l}{dx} - k_l^2E_l\right]e^{i(k_lx-\omega t)}\hat{\mathbf{e}}_l + c.c. =& -\frac{\omega_l^2}{c^2}E_l\hat{\mathbf{e}}_l - \frac{\omega^2}{c^2}\overline{\overline{\chi}}^{(1)}(\omega_l;\omega_l)\cdot\hat{\mathbf{e}}_lE_le^{i(k_lx-\omega_lt)} \\ &-\sum_n\sum_m\frac{\omega_l^2}{c^2}\overline{\overline{\overline{\chi}}}^{(2)}:\hat{\mathbf{e}}_n\hat{\mathbf{e}}_mE_nE_me^{i(k_lx-\omega_lt)} + c.c. \\ =& -\frac{\omega_l^2}{c^2}\left[\overline{\overline{\epsilon}}(\omega_l;\omega_l)\cdot\hat{\mathbf{e}}_lE_le^{i(k_lx-\omega_lt)}\right] \\ &+\sum_n\sum_m\overline{\overline{\overline{\chi}}}^{(2)}:\hat{\mathbf{e}}_n\hat{\mathbf{e}}_mE_nE_me^{i(k_lx-\omega_lt)} + c.c.,\end{aligned} \tag{26}$$

where $\overline{\overline{\epsilon}} = \overline{\overline{1}} + \overline{\overline{\chi}}^{(1)}(\omega_l;\omega_l)$.

Taking the inner product of $\hat{\mathbf{e}}_l^*$ on both sides of the equation and considering that $\hat{\mathbf{e}}_l^*\cdot\hat{\mathbf{e}}_l = 1$, we get

$$\begin{aligned}-k^2E_le^{i(k_lx-\omega_lt)} + 2ik_l\frac{dE_l}{dx} =& -\frac{\omega_l^2}{c^2}\Bigg[\hat{\mathbf{e}}^*\cdot\overline{\overline{\epsilon}}\cdot\hat{\mathbf{e}}_lE_le^{i(k_lx-\omega_lt)} \\ &+\sum_n\sum_m\hat{\mathbf{e}}_l^*\cdot\overline{\overline{\overline{\chi}}}^{(2)}:\hat{\mathbf{e}}_n\hat{\mathbf{e}}_mE_nE_me^{i(k_n+k_m-k_l)x}\Bigg].\end{aligned} \tag{27}$$

The term $\hat{\mathbf{e}}_j^* \cdot \overline{\overline{\epsilon}}(\omega_l;\omega_l)\hat{\mathbf{e}}_l$ corresponds to the square of the refractive index of ω_l, so the wave vector is

$$\begin{aligned} k_l^2 &= \frac{\omega_l^2 n^2(\omega_l)}{c^2} \\ &= \frac{\omega_l^2}{c^2}\hat{\mathbf{e}}_l^* \cdot \overline{\overline{\epsilon}}(\omega_l;\omega_l)\cdot\hat{\mathbf{e}}_l, \end{aligned} \tag{28}$$

then,

$$2ik_l\frac{dE_l}{dx} = -\frac{\omega_l^2}{c^2}\sum\sum\left[\hat{\mathbf{e}}_l^* \cdot \overline{\overline{\chi}}^{(2)}(\omega_l;\omega_n\omega_m) : \hat{\mathbf{e}}_n\hat{\mathbf{e}}_m\right]E_nE_m e^{ix(k_n+k_m-k_l)}. \tag{29}$$

Defining an effective nonlinear coefficient as $\chi_{eff}^{(2)} \equiv \hat{\mathbf{e}}_l^* \cdot \overline{\overline{\chi}}^{(2)}(\omega_l;\omega_n,\omega_m) : \hat{\mathbf{e}}_n\hat{\mathbf{e}}_m$, the last equation is rewritten as

$$\frac{dE_l}{dx} = \frac{i\omega_l}{2n_lc}\sum\sum\chi_{eff}^{(2)}(\omega_l;\omega_n;\omega_m)E_nE_m e^{ix(k_n+k_m-k_l)}, \tag{30}$$

By this way the coupled equations are obtained:

$$\frac{dE_1(x)}{dx} = \frac{i\omega_1}{2cn_1}\chi_{ef}^{(2)}E_3(x)E_2^*(x)exp(i\Delta kx), \tag{31}$$

$$\frac{dE_2(x)}{dx} = \frac{i\omega_2}{2cn_2}\chi_{ef}^{(2)}E_3(x)E_2^*(x)exp(i\Delta kx), \tag{32}$$

$$\frac{dE_3(x)}{dx} = \frac{i\omega_3}{2cn_3}\chi_{ef}^{(2)}E_1(x)E_2(x)exp(-i\Delta kx), \tag{33}$$

where $\Delta k = k_3 - k_1 - k_2$. Each equation describes the rate of change of the amplitude of one of the three interacting waves in terms of the other two.

2.3 Solution of the coupled equations in the undepleted pump approximation: optical parametric amplification

We now solve the coupled wave equations for the special case of optical parametric amplification. Here we identify the electric field amplitude E_3 with the amplitude of the pump wave and E_1 and $E_2$with the signal and idler amplitudes, respectively. For simplicity, we assume that the input intensity of the pump beam is much larger than the intensities of both the signal and idler ($|E_3| \gg |E_2|, |E_1|$), and that the coupling is low enough such that we can assume that pump is not depleted so that the amplitude of the pump wave is approximately constant. For this case, only Eqs. 31 and 32 need

to be solved. We introduce a change of variables to simplify the solution of these equations. Let $A_l = E_l\sqrt{n_l/\omega_l}$. The pair of coupled equations to be solved is then

$$\frac{dA_s}{dx} = i\gamma A_p A_i^* e^{i\Delta kx}, \tag{34}$$

$$\frac{dA_i}{dx} = i\gamma A_p A_s^* e^{i\Delta kx}, \tag{35}$$

where $\gamma = \frac{\chi^{(2)}_{eff}}{2c}\sqrt{\frac{\omega_s\omega_i\omega_p}{n_s n_i n_p}}$ is the coupling constant and, $\Delta k = k_p - k_s - k_i$.

Assuming perfect phase-matching, that is, $\Delta k = 0$, the solutions of Eqs. 34 and 35 are given by

$$A_s(x) = A_s(0)cosh(hx) + iA_i^*(0)sinh(hx) \tag{36}$$

$$A_i(x) = A_i(0)cosh(hx) + iA_s^*(0)sinh(hx). \tag{37}$$

where $h = \gamma A_p(0)$. If we assume $A_i(0) = 0$, then

$$|A_s(x)|^2 = |A_s(0)|^2 cosh^2(hx) \tag{38}$$

$$|A_i(x)|^2 = |A_i(0)|^2 sinh^2(hx). \tag{39}$$

Since the intensity is proportional to the magnitude square of the amplitude, then the previous Eqs. (38) and (39) describe how the intensity of the signal and idler increase as they propagate through the medium. However, the variables A_s and A_i are not exactly the amplitudes of the electric fields, but rather the electric fields normalized by a factor that depends on the frequency and refractive index of the waves. It can be shown that $|A(x)|^2$ is actually proportional to the number of *photons* generated per unit time. If $hx \gg 1$, then

$$|A_s(x)|^2 \approx \frac{1}{4}|A_s(0)|^2 e^{2hx}, \tag{40}$$

$$|A_i(x)|^2 \approx \frac{1}{4}|A_i(0)|^2 e^{2hx}; \tag{41}$$

in other words, the growth of the number of signal photons is the same as the growth of the idler photons. For every pump photon that is anhilated, a pair of signal and idler photons is created.

According to Eqs. (40) and (41), the intensity of both the signal and idler beams

increases without limit with the interaction length, as shown in Fig. (10). This is valid only if the pump can be considered approximately constant throughout the medium. If the intensities of the signal and idler become comparable to that of the pump wave, the signal and idler waves deplete the pump wave; the analysis that has been presented, which supposes that there is no pump depletion, is no longer valid.

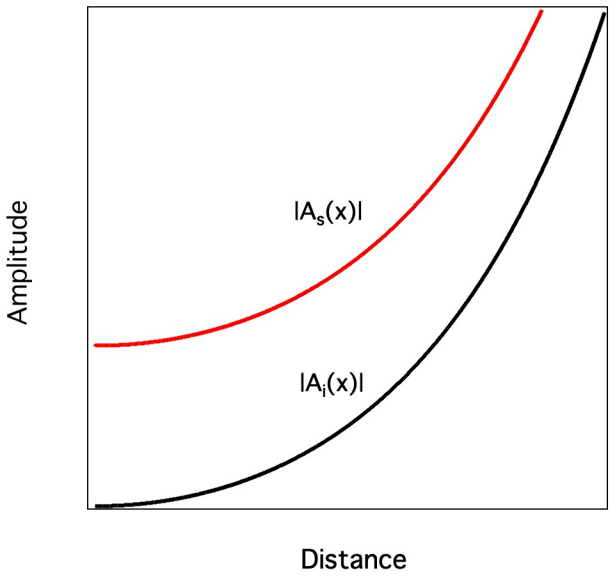

Figure 10. Signals and idlers intensities according to Eqs. (38) and (39).

2.4 Quasi-phase matching

In the previous chapter was explained that to achieve quasi-phase matching a modulation of the non-linearity is required. This modulation is included in the set coupled equations as a spatial dependence in the nonlinearity

$$\frac{dE_s(x)}{dx} = \frac{i\omega_s}{2cn_s}\chi^{(2)}(x)E_p(x)E_i^*(x)e^{i\Delta kx}, \tag{42}$$

$$\frac{dE_i(x)}{dx} = \frac{i\omega_i}{2cn_i}\chi^{(2)}(x)E_p(x)E_s^*(x)e^{i\Delta kx}, \tag{43}$$

$$\frac{dE_p(x)}{dx} = \frac{i\omega_s}{2cn_p}\chi^{(2)}(x)E_s(x)E_i(x)e^{-i\Delta kx}. \tag{44}$$

The $e^{i\Delta kx}$ factor is associated with the dephasing among the generated waves trough the medium. The dynamics of a nonlinear process is described as a result of the interference of these waves. The distance where the waves interfere constructively is

known as coherence length (l_c) and is given by

$$l_c = \frac{\pi}{|\Delta k|}. \tag{45}$$

If a 180° phase shift is added to these waves every coherence length there will be constructive interference. One way to introduce this 180° phase shift is by flipping the sign of the nonlinearity $\chi^{(2)}$.

In the case of ferroelectrics, particularly the lithium niobate crystal which properties are described in next chapter, the tensor of the susceptibility is proportional to the third-order susceptibility tensor and the spontaneous polarization $\mathbf{P}_s$, as follows:

$$\overline{\overline{\chi}}^{(2)} \propto \overline{\overline{\chi}}^{(3)} \cdot \mathbf{P_s} \tag{46}$$

From this equation it can be seen that a change in the spontaneous polarization implies a change in the second order susceptibility. If the direction of $\mathbf{P}_s$ is reversed then the signs in the tensor $\overline{\overline{\chi}}^{(2)}$ are also reversed without any change in their magnitudes.

According to the definition of coherence length in equation (45), and from the mis-match vector, we get:

$$|k_p - k_s - k_i| = \frac{\pi}{l_c}, \tag{47}$$

or

$$\left|\frac{n_p}{\lambda_p} - \frac{n_s}{\lambda_s} - \frac{n_i}{\lambda_i}\right| = \frac{1}{\Lambda}, \tag{48}$$

considering $\Lambda = 2l_c$ as the period of the flipping of $\mathbf{P}_s$ as shown in Fig. (11).

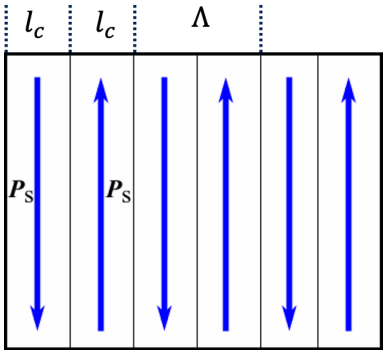

Figure 11. Periodic poling.

Figure (12) shows the spatial variation of the magnitude of the generated field in the nonlinear interaction. Without phase matching, the amplitude of the generated wave field oscillates as the propagation distance increases. In the quasi-phase-matching case, the field amplitude grows monotonically with propagation distance, although less rapidly than in the case of a perfectly phase-matched interaction.

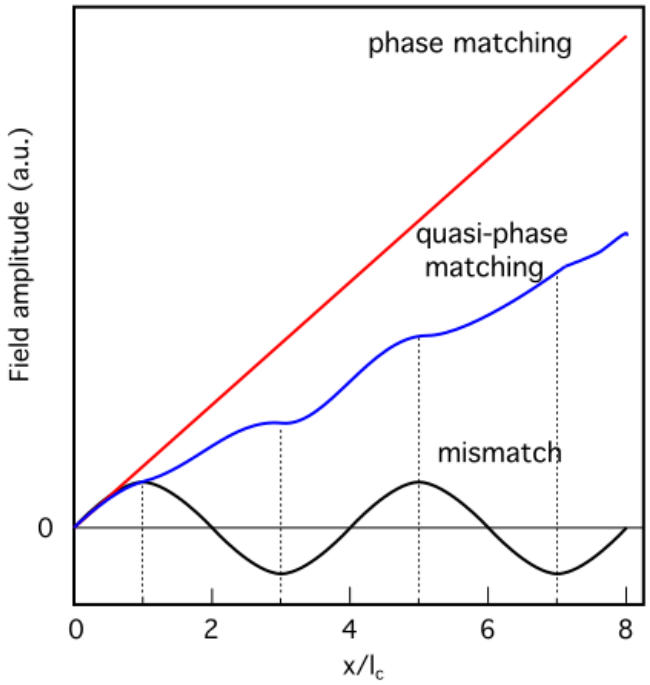

Figure 12. Spatial variation of the field amplitude of the generated signal wave in a nonlinear optical interaction for three different phase matching conditions,

Figure (13) shows the tuning curve for the signal and the idler, according to the period required to generate those wavelengths according to equation (48). The signal of the source developed in this work is centered around 1450 nm and therefore only the interval of periods involved is shown in the graph.

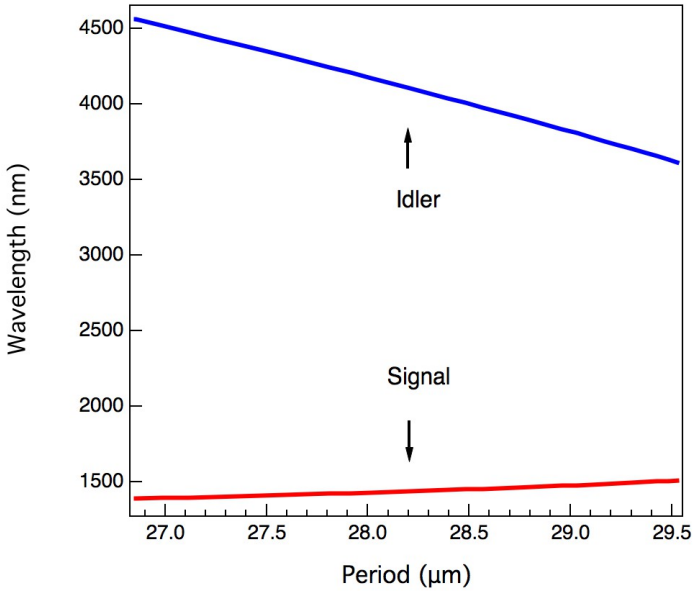

Figure 13. Period required to generate the signal and idler.

From the set of the coupled equations (42-44) and under the assumption of $E_p \approx constant$ and $E_i \approx constant$, the signal field equation is

$$E_s = \frac{i\omega_s}{cn_s} E_p E_i^* \int_0^L \chi^{(2)}(x)\, e^{i\Delta k x} dx. \tag{49}$$

Since the nonlinearity is zero outside the medium we can extend the limits of the integral from $-\infty$ to ∞,

$$E_s \propto \int_{-\infty}^{\infty} \chi^{(2)}(x)\, e^{i\Delta k x} dx. \tag{50}$$

From this equation we can see that the signal field amplitude is proportional to the Fourier Transform of the nonlinearity.

In order to get simultaneously two nonlinear processes in the same medium, which is the objective of this thesis, the magnitude of the Fourier components for both processes must be high, so we need a domain structure such that

$$\chi^{(2)}(\Delta k_j) = \int_{-\infty}^{\infty} \chi^{(2)}(x)\, e^{\Delta k_j x} dx = \mathscr{F}[\chi^{(2)}(x)], \tag{51}$$

is non negligible for the two processes, *j=1,2* (Robles-Agudo and Cudney, 2011).

The domain structure that contains the appropriate Fourier components to obtain

the two nonlinear processes, is given by

$$\chi_{eff}^{(2)}(\Delta k) = \frac{\left|\chi_{33}\right|}{L}\int_0^L g(x)e^{i\Delta kx}dx, \tag{52}$$

where $|\chi_{33}|$ is the magnitude of the highest nonlinearity available of the lithium niobate crystal and the function $g(x)$ contains the two periods to generate both processes and is given by

$$\begin{aligned} g(x) &= sign\left[cos\left(k_1 x\right) - cos\left(k_2 x\right)\right] \\ &= sign\left[cos\left(\frac{2\pi x}{\Lambda_1}\right) - cos\left(\frac{2\pi x}{\Lambda_2}\right)\right]. \end{aligned} \tag{53}$$

Figure (14) shows an example of an aperiodic *g(x)* function, note that period remains constant and there are small variations that introduces a change of phase.

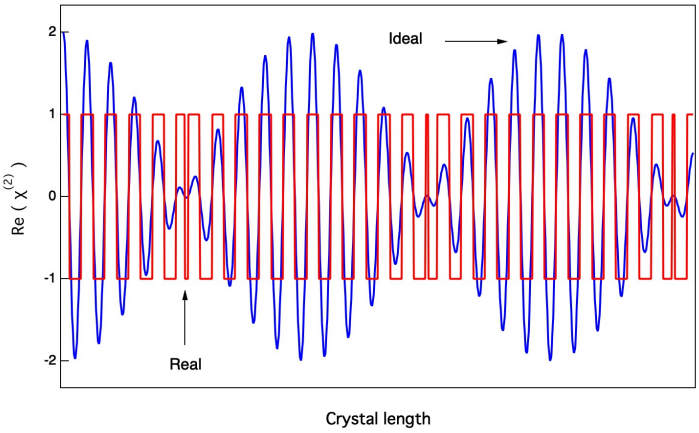

Figure 14. Spatial variation of the nonlinearity. The blue curve is the ideal nonlinearity variation and the red square wave is the real structure achieved

For example, considering a crystals of 50 mm long that has the two periods $\Lambda_1 = 28.51$ and $\Lambda_2 = 28.67$ μm, to generate the two signals $\lambda_{s1} = 1.4482$ and $\lambda_{s2} = 1.4559$ μm, which difference in frequency corresponds to $\delta\omega = 1$ THz, the corresponding Fourier transform obtained by means of the FFT (fast Fourier transform), with a resolution of 100 nm, is shown in Figure (15 a), for a periodic (in blue) and an aperiodic medium (in red); in this figure three groups of maximums appear. Figure (15 b) shows a close up to the first group in $\Delta k \approx 35$ μm^{-1}, it is observed that two large components are much larger than all the other spatial frequency components, looking this graph

is clear that in the aperiodic case the peaks are larger and narrower. Note that in the aperiodic case, there appear two *satellite* peaks besides the main peaks while in the periodic case there are not.

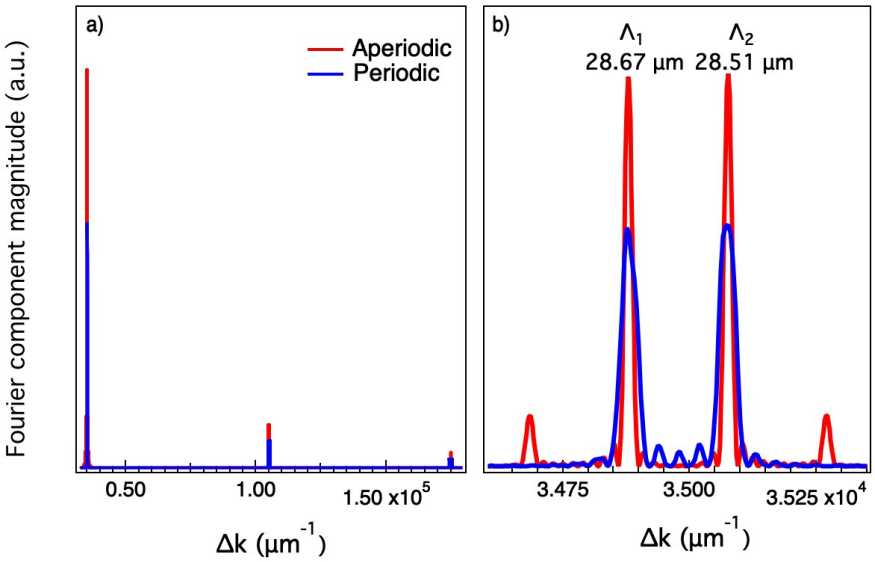

Figure 15. Fourier component magnitude, a) periodic and aperiodic structure. In b) a close-up of the largest magnitude group is shown.

In preliminary experiments we used a crystal with a length of 3.5 cm, the magnitudes of the Fourier components are shown in the red graph of Fig. (16), the final experiments were performed with a crystal with a length of 5 cm. We observe that using longer crystals we get a higher efficiency and narrower bandwidths, as expected.

Since the aperiodic structure only generates two processes, the Eq. (53) can be written as

$$g(x) = sign\left[sin\left(\overline{k}x\right) sin\left(\frac{\pi x}{D}\right)\right] \tag{54}$$

where, $\overline{k}$ is the average of k_1 and k_2, and $D = 2\pi/\delta k = \left(\frac{\Lambda_1\Lambda_2}{\Lambda_1-\Lambda_2}\right)$. Considering this equation, the integral in Eq. (52) can be is splitted in a sum of integrals whose limits of integration vary according to D and is given by

$$\begin{aligned}\int_L^0 g(x)e^{i\Delta kx}dx &= \int_0^D g(x)e^{i\Delta kx}dx + \int_D^{2D} g(x)e^{i\Delta kx}dx + \ldots + \int_{(M-1)}^{MD} g(x)e^{i\Delta kx}dx \\ &= \sum_{l=0}^{M-1}\int_{lD}^{(l+1)D} g(x)e^{i\Delta kx}dx.\end{aligned} \tag{55}$$

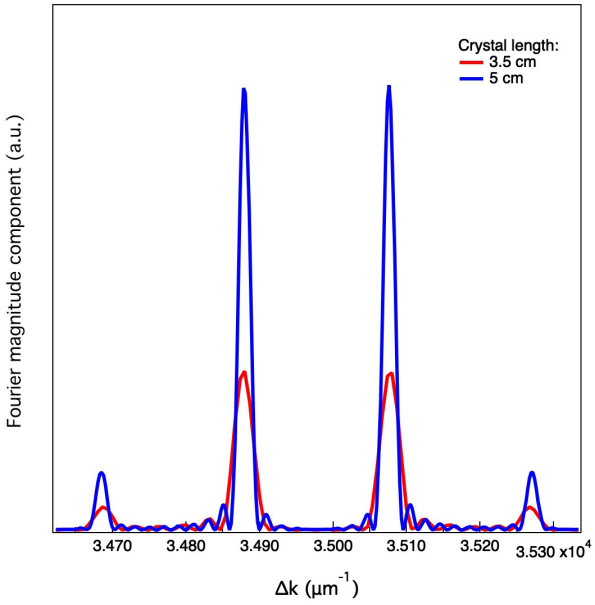

Figure 16. Fourier component magnitude in an aperiodic structure in crystals with different lengths

Considering that the sign of g(x) flips according to the structure we can get

$$\begin{aligned}\int_{lD}^{(l+1)D} g(x)e^{i\Delta kx}dx &= (-1)\left[\int_{lD}^{lD+d} e^{\Delta kx}dx - \int_{lD+d}^{lD+2d} e^{\Delta kx}dx + \int_{lD+2d}^{lD+3d} e^{\Delta kx}dx - \ldots\right] \\ &= (-1)^l \sum_{j=0}^{N-1}\left[\int_{lD+j\Lambda}^{lD+(j+1/2)\Lambda} e^{i\Delta kx}dx - \int_{lD+(j+1)\lambda}^{lD+(j+1)\lambda} e^{i\Delta kx}\right] \\ &= (-1)^l \sum_{j=0}^{N-1}\left[e^{i\Delta kx}\Big|_{lD+j\Lambda}^{lD+(j+1/2)\Lambda} - e^{i\Delta kx}\Big|_{lD+(j+1/2)\Lambda}^{lD+(j+1)\Lambda}\right],\end{aligned} \tag{56}$$

where $\Lambda = \frac{2\pi}{\bar{k}} = \frac{4\pi}{(k_1+k_2)}$.

It can be shown that the solution is given by

$$\left|\chi^{(2)}_{eff}(\Delta k)\right| = \chi_{33}\left|\frac{2}{\Delta kL} tan\left(\frac{\Delta k\Lambda}{4}\right) tan\left(\frac{\Delta kD}{2}\right) cos\left(\frac{\Delta kL}{2}\right)\right|. \tag{57}$$

The magnitude of the effective nonlinearity given in Eq. (57), normalized to $\chi^{(2)}_{33}$, is plotted in Fig. (17), in the Appendix more details are provided. In both analysis, using the FFT shown in Fig.(15) and in the analytic solution shown in Fig. (17), two peaks appear besides of the main peaks, while in the periodic case they do not appear, this means that this aperiodic design will favor the appearance of *satellite* peaks next to each signal, as is presented in Chapter of experiment and results.

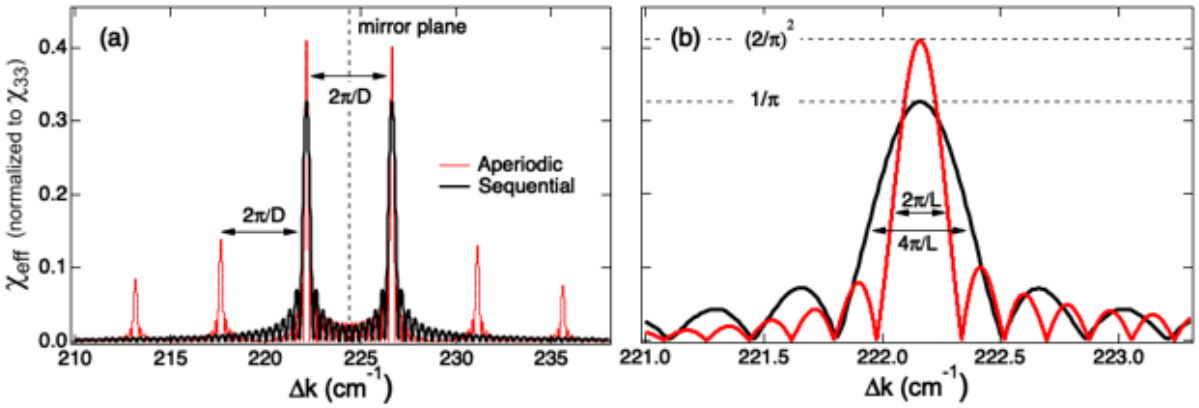

Figure 17. Effective nonlinearities of aperiodic and sequentially periodic structures. a) large scale that shows the secondary peaks of the aperiodic structure; b) close-up of one of the two main peaks. Values used in the simulation: Λ_1 = 28μm, D = 150μm, L = 35mm

Chapter 3. Physical properties of lithium niobate and design of the aperiodical poled gratings

In this chapter the physical properties of lithium niobate ($LiNbO_3$) crystal are described. This crystal is widely used in waveguides, integrated optics, and in nonlinear optics because of its optical properties. For the objective of this work the most important property is its ferroelectricity since it is used to implement the quasi-phase matching.

The fabrication of the aperiodically poled crystals is presented in detail.

3.1 Physical properties of lithium niobate crystal

Lithium niobate ($LiNbO_3$) is a birefingent, uniaxial and ferroelectric nonlinear crystal. This crystal is transparent for wavelengths from 350 to 5200 nm, Fig. (18) shows the absorption coefficient of the entire window (Leidinger *et al.*, 2015). One advantage of the quasi-phase matching (QPM) is that it can be achieved within the entire transparency range of the nonlinear crystal. On the other hand, a disadvantage of quasi-phase matching is that a change of their spectral shape is not possible once the design and fabrication processes are completed. Birefingence is the optical property where the refractive index depends on the polarization direction. It is also defined as the difference between the ordinary and the extraordinary refractive index ($n_e - n_o$) at some wavelength. $LiNbO_3$ has a negative birefringence, which means $n_e < n_o$. Moreover, refractive indexes are associated with the direction of the axes: $n_x = n_o$, $n_y = n_o$ and $n_z = n_e$.

The coordinate system used to describe the physical properties of this crystal is the cartesian system *x, y, z*. The *c*-axis of the crystal (crystallographic axis) is defined as the intersection of the symmetry planes and is parallel to the *z* axis; it can be positive or negative and the orientation is determined by its pyroelectic nature. When the crystal is heated the temperature change causes the lithium and niobium ions to move in the direction of the *c*-axis with respect to their original positions, producing an excess of negative charge on one of the faces of the crystal, which generates a voltage between the two *c*-faces of the crystal. The $+c$-face is defined as the one that becomes positive upon cooling (Weis and Gaylord, 1985).

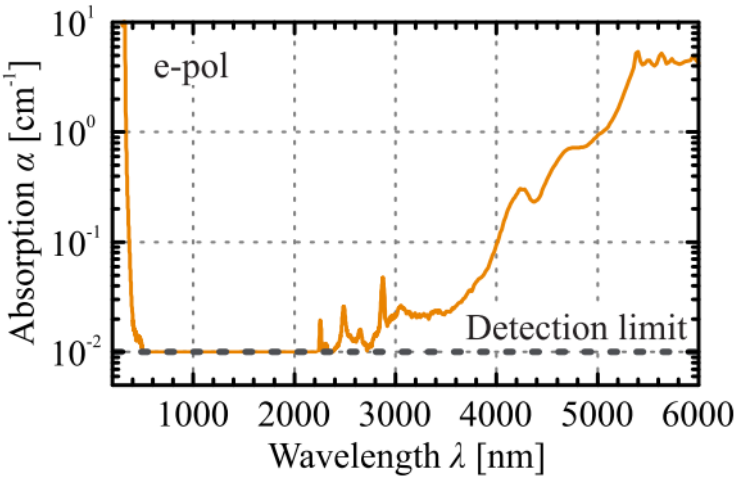

Figure 18. Absoption coefficient in lithium niobate crystal.

This crystal exhibits three-fold rotation symmetry about its *c* axis, as shown in Fig. (19). Thus, it is a member of the trigonal crystal system; it exhibits mirror symmetry about three planes that are 120° apart and intersect forming a three-fold rotation axis. These axes are defined as the *x*-axes. The crystal is a member of the *3m* point group. The crystaline structure is shown in Fig. (20).

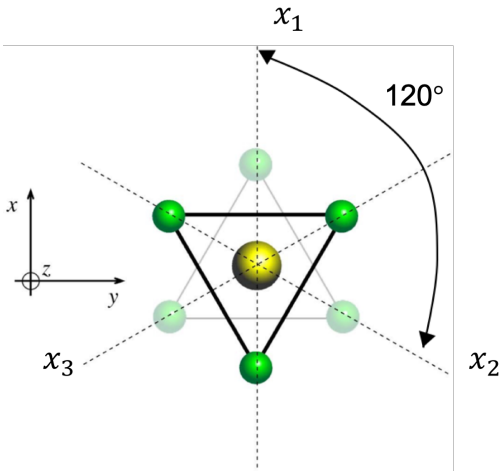

Figure 19. Cristalographic axis in the $LiNbO_3$

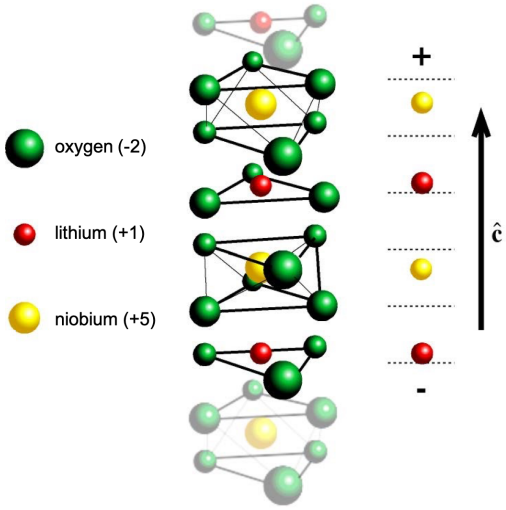

Figure 20. Lithium niobate crystaline structure.

Other properties of lithium niobate such as: the absorption coefficient, refractive index, the coercive field; depend on its stoichiometry, that is the Li/Nb ratio. In our experiments we use $LiNbO_3$ wafers with a congruent stoichiometry, where Li/Nb=0.946.

The extraordinary refractive index follows the Sellmeier equation given by

$$n_e^2 = a_1 + b_1 f + \frac{a_2 + b_2 f}{\lambda^2 - (a_3 + b_3 f)^2} + \frac{a_4 + b_4 f}{\lambda^2 - a_5^2} - a_6 \lambda^2, \tag{58}$$

the coefficients values are $a_1 = 5.35583$, $a_2 = 0.100473$, $a_3 = 0.20692$, $a_4 = 100$, $a_5 = 11.34927$, $a_6 = 1.5334 \times 10^{-2}$, $b_1 = 4.692 \times 10^{-7}$, $b_2 = 3.862 \times 10^{-8}$, $b_3 = -0.89 \times 10^{-8}$, $b_4 = 2.657 \times 10^{-5}$ and $f = (T - 24.5)(T + 520.82)$ (Jundt, 1997), where T is the temperature (°C).

In Chapter (1) was explained that ferroelectric materials have an intrinsic dipole moment known as the spontaneous polarization $\mathbf{P}_s$, which can be switched when a strong electric field is applied for some time. These crystals posses at least two equilibrium orientations of the spontaneous polarization vector in the absence of an external electric field. This vector may be switched between those orientations by an external electric field. The magnitude of the electric field that changes the direction of polarization is known as the *coercive field*, E_c. The process is ideally illustrated in Fig. (21), but the real shape of the loop is affected by different factors such as the crystal thickness, the presence of charged defects, mechanical stresses, preparation conditions, and thermal treatment. The regions of the crystal with uniformly oriented spontaneous polarization are known as *ferroelectric domains* and the region between two domains is a domain wall. The walls that separate domains with oppositely oriented polarization are called 180° walls (Wojde and Íñiguez, 2014), which is the case in this work.

Ferroelectric crystals posses a permanent polarization, known as the spontaneous polarization $\mathbf{P}_s$ In ferroelectric materials, the second order nonlinear coefficient $\chi^{(2)}$ is proportional to the third order tensor according to (DrDomenico and Wemple, 1969):

$$\overline{\overline{\chi}}^{(2)} \propto \overline{\overline{\overline{\chi}}}^{(3)} \cdot \mathbf{P}_s. \tag{59}$$

From this equation it can be seen that a change in the spontaneous polarization implies a change in the second order susceptibility. If the direction of $\mathbf{P}_s$ is reversed then the signs in the tensor $\overline{\overline{\chi}}^{(2)}$ are also reversed without any change in their magnitudes.

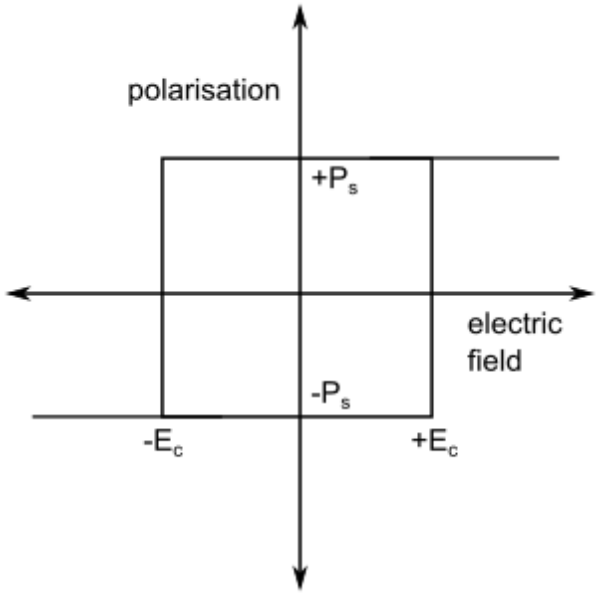

Figure 21. Ideal ferroelectric hysteresis.

3.2 Effective nonlinear susceptibility

For a particular crystal, the forms of the linear and nonlinear optical susceptibilities are determined by the symmetry properties. For this reason, it is necessary to determine what types of symmetry properties can occur in a crystalline medium, which depends on the point group to which it belongs. As was mentioned before, $LiNbO_3$ belongs to the 3m point group.

The effective nonlinearity is given by

$$\chi_{eff}^{(2)} = \hat{\mathbf{e}}_p^* \cdot \overline{\overline{\chi}}^{(2)}\left(\omega_p; \omega_s, \omega_i\right) : \hat{\mathbf{e}}_s \hat{\mathbf{e}}_i, \tag{60}$$

where $\hat{\mathbf{e}}_p$, $\hat{\mathbf{e}}_s$ and, $\hat{\mathbf{e}}_i$ are unit vectors of the pump, signal and, idler polarization states and $\overline{\overline{\chi}}^{(2)}\left(\omega_p; \omega_s, \omega_i\right)$ is the second order nonlinear tensor corresponding to the pump, signal and idler frequencies.

The nonzero tensor elements for the point group of the $LiNbO_3$ are

Tensor elements	Compact notation
$\chi_{xxz}^{(2)}=\chi_{xzx}^{(2)}=\chi_{zxx}^{(2)}=\chi_{zyy}^{(2)}=\chi_{yzy}^{(2)}=\chi_{yyz}^{(2)}$	$\chi_{31}^{(2)}$
$\chi_{xyx}^{(2)}=\chi_{xxy}^{(2)}=\chi_{yxx}^{(2)}=-\chi_{yyy}^{(2)}$	$\chi_{22}^{(2)}$
$\chi_{zzz}^{(2)}$	$\chi_{33}^{(2)}$

In lithium niobate, the magnitude of these tensors are $|\chi_{31}| \approx 5.1 \times 10^{-12}$ m/V, $|\chi_{22}| \approx 2.46 \times 10^{-12}$ m/V and, $|\chi_{33}| \approx 27 \times 10^{-12}$ m/V.

The effective nonlinearity is given by

$$\begin{aligned}\chi_{ef}^{(2)} &= \hat{\mathbf{z}} \cdot [(\hat{\mathbf{x}}\hat{\mathbf{x}}\hat{\mathbf{z}} + \hat{\mathbf{x}}\hat{\mathbf{z}}\hat{\mathbf{x}} + \hat{\mathbf{z}}\hat{\mathbf{x}}\hat{\mathbf{x}} + \hat{\mathbf{z}}\hat{\mathbf{y}}\hat{\mathbf{y}} + \hat{\mathbf{y}}\hat{\mathbf{z}}\hat{\mathbf{y}} + \hat{\mathbf{y}}\hat{\mathbf{y}}\hat{\mathbf{z}})\chi_{31} \\ &\quad + (\hat{\mathbf{x}}\hat{\mathbf{y}}\hat{\mathbf{x}} + \hat{\mathbf{x}}\hat{\mathbf{x}}\hat{\mathbf{y}} + \hat{\mathbf{y}}\hat{\mathbf{x}}\hat{\mathbf{x}} - \hat{\mathbf{y}}\hat{\mathbf{y}}\hat{\mathbf{y}})\chi_{22} + \hat{\mathbf{z}}\hat{\mathbf{z}}\hat{\mathbf{z}}\chi_{33}] : \hat{\mathbf{z}}\hat{\mathbf{z}} \\ &= \chi_{33}^{(2)}.\end{aligned} \tag{61}$$

Thus, when the three interacting waves have extraordinary polarization, which is the case of this work, the largest available nonlinearity χ_{33} is used . However, if all waves have the same polarization state, it is not possible to achieve phase matching, because the refractive index are different for each wave. In order to access to χ_{33}, it is necessary to implement the quasi phase matching (QPM). As previously explained, QPM allows us to design a crystal with two different periods to generate two processes. The design and manufacturing process of the APLN that was made to generate two non-linear processes is described below.

3.3 Design and fabrication of the aperiodically poled lithium niobate

Once we have calculated the required periods Λ_1 and Λ_2, the first step is to fabricate a mask in an holographic film that contains the information of the periods to be transfered to the crystal. A green diode laser ($\lambda = 532$ nm) passes through a spatial filter and then illuminates a slit. The image of the slit is then projected by a lens in the holographic film. The film is held in a translation stage, the stage moves laterally according to the information of the periods, and a pattern of stripes is formed. The translational stage has a spatial resolution of ≈ 100 nm; the experimental set up is illustrated in Fig. (22).

Once the mask is ready it is transferred onto the crystal. A 2 μm thick photoresist layer is deposited on the positive face of the crystal ($+c$). The mask is placed on the photoresist layer then exposed to ultraviolet light and developed. The pattern obtained in the photoresist is shown in Fig. (23 a). To create the ferroelectric domains, the crystal is immersed in an electrolyte solution (H_2O:LiCl) as shown in Fig. (23 b). A high voltage is applied in order to drive the electric field above the coercive field. The

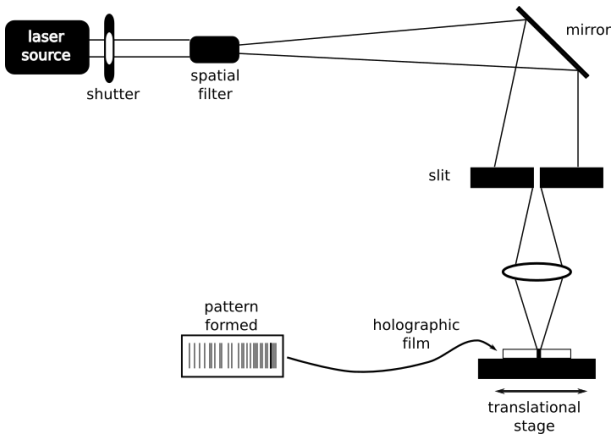

Figure 22. Mask fabrication set up.

voltage that is required is $V \geq dE_c$, where d is the thickness of the crystal. The electric field E_c induces the nucleation of domains on the surface where the photoresist is; the domains spread to the other surface and then grow laterally.

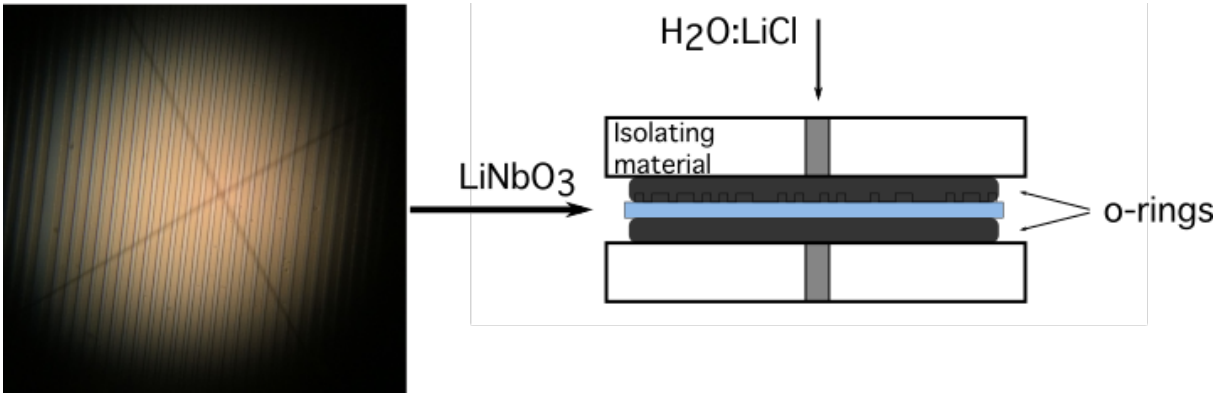

Figure 23. Process of ferroelectric domain inversion. In a) the aperiodical pattern is transferred in the photoresist; b) crystal immersed in an electrolyte solution to create the ferroelectric domains.

Figure (24 a) shows the domains created in the $LiNbO_3$ sample, seen through a microscope and using crossed polarizers. The crystal is then heated at 150° C for one hour to eliminate the stress produced. Figure (24 b) shows the domains created, this image was obtained through a phase contrast microscope, the images are not at the same scale. The crystal is cutted, polished and antirreflection films are deposited on its faces to minimize losses due to reflections.

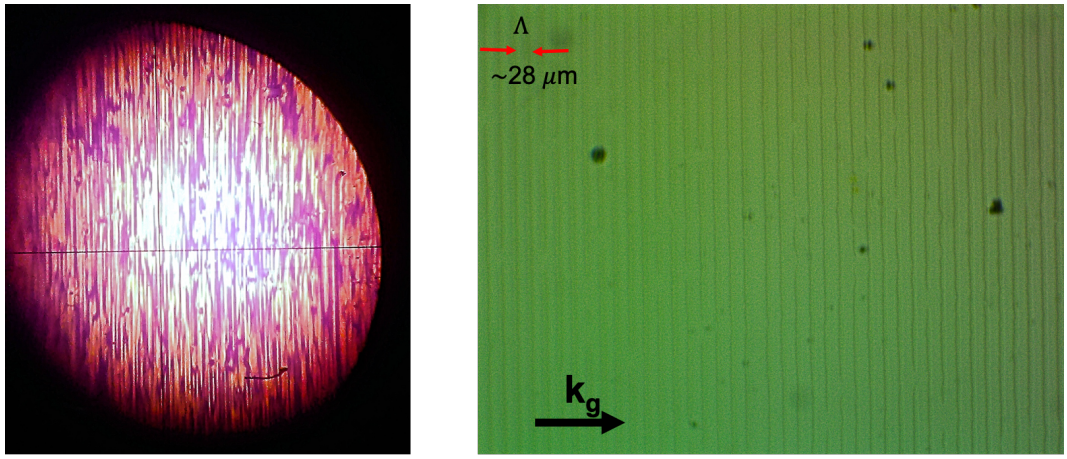

Figure 24. Experimental images from: a) ferroelectric domains seen through crossed polarizers and, b) ferroelectric domains seen through phase contrast microscope once the crystal was heated.

Chapter 4. Theory of terahertz generation by difference frequency generation

The wave equation given in Chap. 2 by the Eq.(18) is a particular case of the more general equation given by

$$\nabla^2\mathbf{E} - \frac{1}{c^2}\frac{\partial^2\mathbf{E}}{\partial t^2} = \mu_0\frac{\partial^2\mathbf{P}}{\partial t^2} + \frac{\partial\mathbf{j}}{\partial t}, \tag{62}$$

in the right side of the equation we have two terms that correspond to the sources. This means that the electric field can be generated by a temporal variation of the local current density **j**, or by modulating the local polarization **P**. In the first case, THz radiation is carried out with free electrons in devices such as particle accelerators, free electron lasers or synchronous radiation sources. In the case of the polarization modulation there are two options: one with a resonance character, and the other based on non-resonant modulation of **P**.

Resonance polarization effects are: photoconductive emitters and photo-mixers (which are the photoconductive emitters), semiconductor surface emitters (where visible femtosecond lasers illuminate a semiconductor surface and it emits electromagnetic transient in the THz range), intramolecular photo induced-change transfer (where a femtosecond laser excites molecules aligned into a crystal lattice and, the microscopic currents form a macroscopic current that generates a THz-range electromagnetic wave), ionized gases (where intrinsic vibrations of laser plasma, produced under the gas ionization by high-power laser pulses, lead to a high-power THz radiation). Non-resonance polarization effects are: difference frequency generation and THz parametric oscillation, optical rectification and tilted pulse front (Kitaeva, 2008). The experiments developed in this work were focus in generate terahertz radiation by difference frequency generation. The pump beams correspond to the pair of signals generated by the OPO and the OPG experiments and they are mixed in the organic crystal: quinolinium salt HMQ-TMS (2-(4-hydroxy-3-methoxystyryl)-1-methylquinolinium-2,4,6-trimethylbenzenesulfonate).

Terahertz frequency generation based in difference frequency generation (DFG) requires the that the difference in frequency of the two electric fields of the signals is required to be such that $\omega_{THz} = \omega_{s1} - \omega_{s2}$. A simple picture of DFG is illustrated in

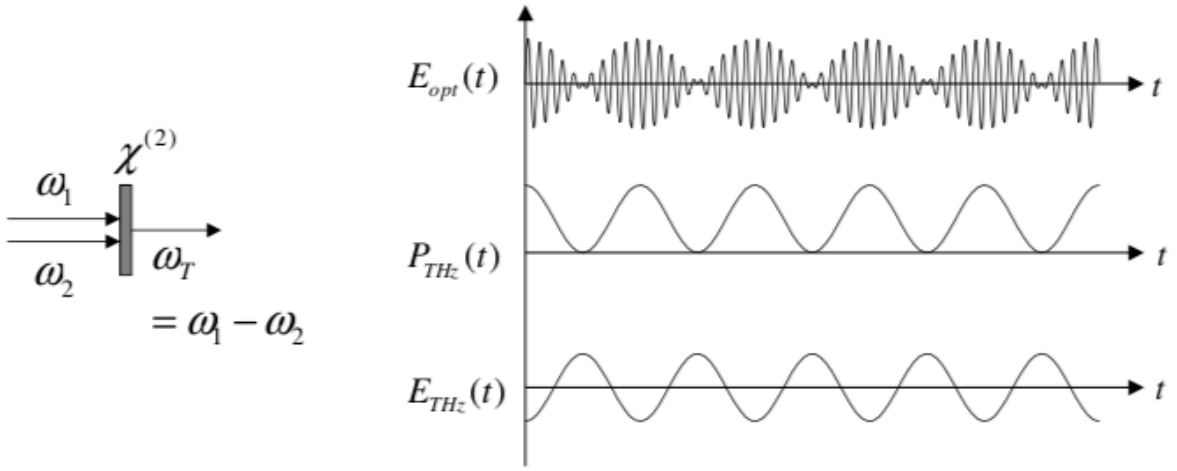

Figure 25. Schematic diagram of difference frequency generation in a thin nonlinear crystal.

Fig. (25). DFG is a second-order nonlinear optical process; thus it requires a non-centrosymmetric crystal. In our experiments we use the organic crystal HMQ-TMS. When the optical beams propagate collinear and are linearly polarized in the same direction, their interference manifests a beat, which oscillates with the difference frequency or beat frequency ($\omega_{THz} = \omega_{s1} - \omega_{s2}$):

$$\begin{aligned} E_O(t) = E_{s1}(t) + E_{s2}(t) &= E_0(sin\omega_1 t + sin\omega_2 t) \\ &= 2E_0 cos\left(\frac{\omega_{THz}}{2}t\right) sin\omega_O t, \end{aligned} \tag{63}$$

where $\omega_O = (\omega_{s1} + \omega_{s2})/2$ is the average optical frequency. The second-order nonlinear polarization of DFG is proportional to the beat intensity:

$$P_{THz}(t) = \chi^{(2)} E_0^2 \left[cos\left(\frac{\omega_{THz}}{2}t\right)\right]^2 = \frac{1}{2}\chi^{(2)} E_0^2 \left[1 + cos(\omega_{THz} t)\right]. \tag{64}$$

Consequently, the THz radiation field induced by the nonlinear polarization is given by

$$E_{THz}(t) \propto \frac{\partial^2 P_{THz}(t)}{\partial t^2} = -\frac{1}{2}\chi^{(2)} \omega_{THz}^2 E_0^2 cos\omega_{THz} t. \tag{65}$$

The THz field oscillates at the difference frequency, ω_T (Lee, 2009).

Similar to the coupled Eqs. (31)-(33) the set of equations that describes the DFG interaction is given by

$$\frac{dA_{s1}}{dx} = \frac{2id_{eff}\omega_{s1}}{\epsilon_0 c n_{s1}} A_{s2} A_{THz} e^{-i\Delta k x}, \tag{66}$$

$$\frac{dA_{s2}}{dx} = \frac{2id_{eff}\omega_2}{\epsilon_0 c n_{s2}} A_{s2} A^*_{THz} e^{i\Delta kx}, \tag{67}$$

$$\frac{dA_{THz}}{dx} = \frac{2id_{eff}\omega_{THz}}{\epsilon_0 c n_{THz}} A_{s1} A^*_{s2} e^{i\Delta kx}. \tag{68}$$

When the two optical beams are polarized in the same direction and the dispersion is negligible at ω_{s1} and ω_{s2}, the optical refractive index is $n_O \equiv n_{s1} (\approx n_{s2})$. In this case, the momentum mismatch is given by:

$$\Delta k = \frac{n_O \omega_{s1}}{c} - \frac{n_O \omega_{s2}}{c} - \frac{n_{THz}\omega_{THz}}{c} = \frac{\Delta n \omega_{THz}}{c} \tag{69}$$

If the phase matching condition is satisfied, $\Delta k = 0$, the THz wave copropagates with the beat of the optical beams at the same velocity.

Figure (26 a) shows the value of the group refractive index of the organic crystal HMQ-TMS, it seems that it remains approximately constant for the range of 1450-1500 nm, which are the values that we use in our experiments (Brunner *et al.*, 2014). For efficient conversion from the signals to the THz it is necessary satisfy that $n_{THz} \simeq n_g$. Figure (26 b) shows the value of the refractive index at different THz frequencies.

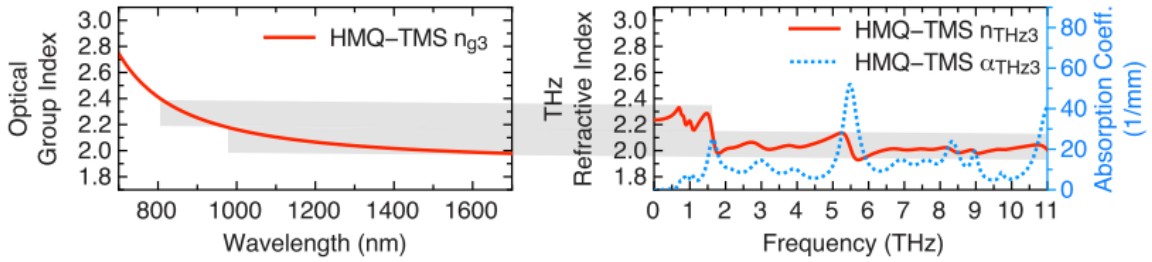

Figure 26. a) HMQ-TMS group index. b) Absorption coefficient

Another important parameter derived from the phase matching condition is the coherence length. When the propagation is collinear, the coherence length is given by

$$\begin{aligned} l_c &= \frac{\pi}{|\Delta k|} \\ &= \frac{1}{2}\left(\frac{n_{THz}}{\lambda_{THz}} - \frac{n_{s1}}{\lambda_{s1}} + \frac{n_{s2}}{\lambda_{s2}}\right)^{-1}. \end{aligned} \tag{70}$$

In the case of very small differences between the refractive index signals, which is our case, the dispersion is given by $n_{s2} = n_{s1} + (\partial n/\partial\lambda)(\lambda_{s2} - \lambda_{s1})$ and the coherence

length is given by:

$$l_c = \frac{\lambda_{THz}}{2(n_{THz} - n_g)}, \tag{71}$$

where n_g is the group index of the signals.

For the wavelengths around 1400 nm, the effective length of the HMQ-TMS is given by the Fig. (27). The crystal provided by Dr. Mojca Jazbinsek has a thick of 0.46 mm. According to the information provided in Fig. (26) the length is enough to achieve efficient phase matching.

The experiments performed using both configurations OPO and OPG, are described in next chapter.

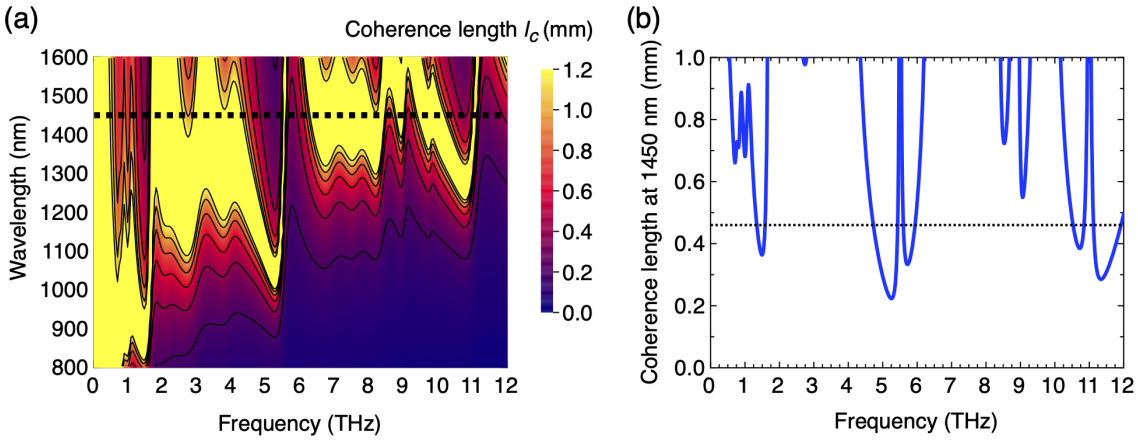

Figure 27. Coherence length for THz generation in HMQ-TMS

The optical properties of organic crystal are briefly described below.

4.1 HMQ-TMS organic crystal

Organic crystals are materials designed for nonlinear optics applications because of its large phase-match nonlinear optical coefficient, mechanical and chemical stability and its high damage threshold. In order to generate nonlinear effects, it is important that the crystals have a non-centrosymmetrical structure. Some of the organic crystals widely used in nonlinear optics are: DAST, DSTMS, OH1, HMQ-T and HMQ-TMS. Our terahertz experiments were performed using a HMQ-TMS crystal, this is a quinolium crystal that has a quinolinium-based ionic-cation core structure. This crystal was first reported in (Jeon *et al.*, 2013), the growth method and the optical and physical

characteristics of the crystal are described. The experiments performed in (Jeon *et al.*, 2013) with the HMQ-TMS crystal were by optical rectification using a Ti:Sapphire amplifier system, with a center wavelength of 800 nm, that delivers 90 fs pulses at a repetition rate of 1 kHz generating THz radiation in the range of 1 to 6 THz.

The crystal structure of HMQ-TMS is shown in Fig. (28). Compared to other organic nonlinear optical crystals, HMQ-TMS shows better environmental stability providing the possibility of an easy control of the crystal thickness and aperture size (Jeon *et al.*, 2013).

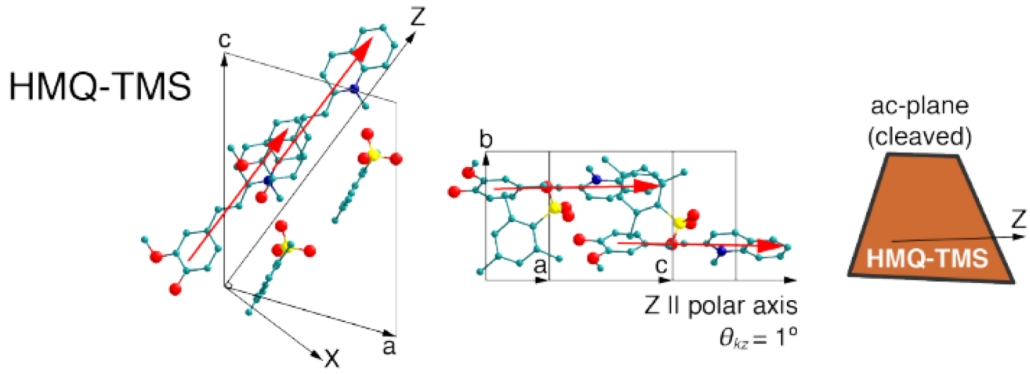

Figure 28. Crystal structure of the organic crystal HMQ-TMS (Jazbinsek *et al.*, 2019)

4.2 Terahertz detection

Depending on their applications and types of circuit for detecting electromagnetic radiation, the detecting systems can also be broadly divided into two groups:

- Incoherent detection systems, which allow only signal amplitude detection.
- Coherent detection systems, which allow detecting not only the signal amplitude, but also its phase.

The choice between coherent or incoherent detection for a given application at a particular THz spectral range is not always obvious and it depends on the application purposes. In the experiments that we have made we use a pyroelectric detector, which corresponds to an incoherent detection system.

Pyroelectric thermal detectors are based on ferroelectric crystals, such as lithium tantalate, which generate a charge as the temperature rises by absorbing THz radia-

tion. The charge results in a current output when is connected to an external electrical circuit, it is directly proportional to the rate of change of temperature of the crystal. It is therefore important to maximize the temperature change through thermal isolation of the crystal and using absorbing coatings with low thermal mass to rapidly transfer heat to the crystal (Rieke, 2003).

4.3 Optical components

Besides lenses and mirrors another important element in the THz radiation are the filters. The most important requirement for filters is to remove all radiation up to a predetermined wavelength and transmit at THz wavelengths. Different materials are used as filters, such as: polyethylene, polypropylene, polystyrene, polytetrafluorethylene, poly-4-methylpentene-1, polyesthylene terephthalate, parylene, fluorgold, zitex, crystaline quartz, sapphire silicon and germanium, diamond, alkali halides, KRS-5 (Kristalle aus dem Schmelzfluss), Fig. (29) shows the absorption coefficient and the transmitance at different THz frequencies (Brundermann *et al.*, 2012).

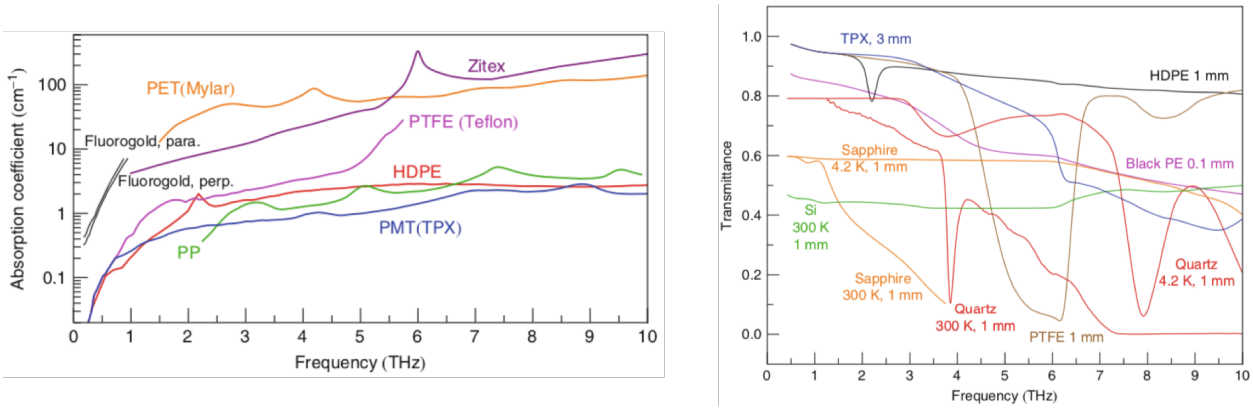

Figure 29. Absorption coefficient and transmittance of fillters commonly used for THz.

Polyethylene (PE or HDPE) is the most generally useful material for THz elements because of its low cost, high transmission, a constant refractive index, additionaly it is mechanically strong. In our experiments we use a $\sim$ 1 mm thick piece of black HDPE, which looks suitable to block the infrared pump pulses and transmits the generated range of THz frequencies.

Chapter 5. Experiments and Results

In this chapter we present the experiments and results with the OPO and OPG sources using the designed APNL crystal to obtain pairs of signals around 1.45 μm, with their corresponding idlers, to generate tunable THz radiation by DFG.

In the OPO configuration, we use as pump source a commercial Nd:YAG laser (λ_p = 1064 nm, the pulse duration τ = 12 ns, the maximum energy of the pulses incident on the crystals is 10 mJ at a repetition rate of 5 Hz). The maximum signals combined energy obtained was 0.740 mJ and the pulse duration ∼ 5 ns. In the OPG configuration we use a home-made Nd:YLF laser with shorter pulses (λ_p = 1047 nm, pulse duration τ ∼ 1.5-1.6 ns, maximum energy supplied is 300 μJ at a repetition rate of 27 Hz). The signals combined energy obtained was 20-38 μJ. The results derived from the two sources based on optical parametric generation (OPG) and oscillation (OPO) are reported in (Carrillo-Fuentes and Cudney, 2019).

Terahertz experiments were performed using both sources OPO and OPG using the organic crystal HMQ-TMS as the mixing medium; it has a high second-order nonlinearity and a refractive index dispersion suitable for obtaining ∼1-10 THz radiation by DFG using signal wavelengths close to 1.45 μm. The detection was made using a pyroelectric sensor. We obtained tunable THz pulses from 1 to 10 THz. The results derived from the experiment performed using OPG source are reported in (Carrillo-Fuentes *et al.*, 2020).

5.1 Optical parametric oscillator design

In one experiment, the APLN sample was placed inside a cavity in order to obtain an OPO. As the pump source, we used a flash lamp pumped Q-switched Nd:YAG laser (12 ns FWHM pulse width; 5 Hz repetition rate). The energy per pulse was varied by a $\lambda/2$ plate and a Glan-Thompson polarizer, and could be set from 0 to 13 mJ. The pump beam was focused on the APLN crystal along with a combination of a spherical (*f=200 mm*) lens and a cylindrical (*f=40 mm*) lens. This configuration allowed us to generate a beam with an elliptical cross section in order to increase the area of the pump beam while maintaining it confined in the 500 μm thick sample. The beam cross-section dimensions were ∼ 0.32 mm and ∼ 1.6 mm (FWHM) parallel and perpendicular to the

c-axis, respectively, therefore the area of the focused pump beam was ~ 4 x 10^{-3} cm^2, so that the maximum fluence we could obtain at 13 mJ was ~ 3.2 J/cm^2, which is approximately the crystal's damage threshold (~ 3 J/cm^2). The crystal was placed in a translation stage in order to change the grating and tune the signal wavelengths.

The cavity of the oscillator consisted of a pair of mirrors; the mirror through which the OPO was pumped (*radius of curvature = 100 mm*) had a 90% reflectivity at 1.45 μm and 80% transmittivity at 1.064 μm. The output coupler was a flat mirror that transmits 60% at 1.45μm and is highly reflective at 1.064 μm. The total length of the cavity is 7 *cm*; the experimental set-up is shown in Fig. (30).

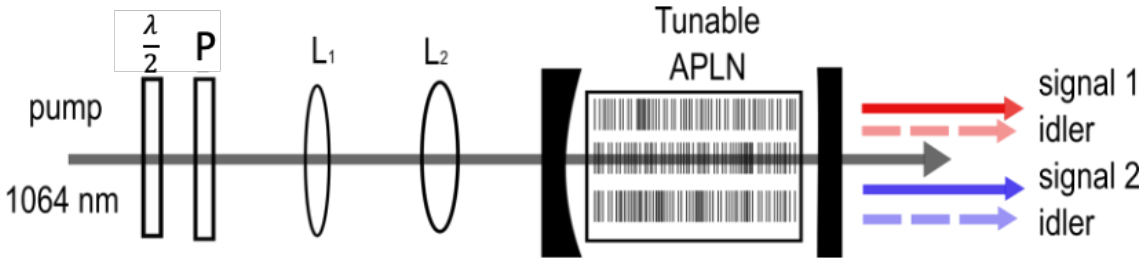

Figure 30. Experimental setup: optical parametric oscillator

The APLN was designed to obtain pairs of signal wavelengths around 1.45 μm with frequency differences ranging from approximately ~ 1 to ~ 10 THz, at room temperature. The poling period, design signal wavelengths, their frequency differences as well as their experimentally obtained values when the APLN sample was placed in the OPO resonator and pumped with the Nd:YAG laser are shown in Table 1. The theoretical calculations of the expected signal wavelengths were performed using the Sellmeier equation for congruently grown lithium niobate given in (Jundt, 1997). All experiments were performed at room temperature.

Figure (31) shows the spectra obtained with Grating 2. Figure 31(a) shows the signals detected with an infrared spectrometer (*f=250 mm* Czerny-Turner, 600 ln/mm grating with a 128 pixel InGaAs array). Two strong peaks of almost equal intensity appear, one centered around 1.454 μm and the other around 1.469 μm; these values are very close to the theoretical predictions, 1.455 and 1.469 μm, shown in Table 1. Each of these peaks has a FWHM of about 0.75 nm, which is close to the resolution of this spectrometer (~100 GHz). Due to the high nonlinearity of the crystal, non-phase-matched sum-frequency generation occurs between the generated signals and the pump wave, creating waves with a wavelength given by $\lambda_R = \lambda_p\lambda_s/(\lambda_p + \lambda_s)$; we

Table 1. Parameters of the APLN sample used in the OPO configuration.

Grating	Period (μm)	Signals λ (μm) theory	Signals λ (μm) experiment	$\Delta\nu$ (THz) theory	$\Delta\nu$ (THz) experiment
1	28.51 28.67	1.4498 1.4576	1.4480 1.4565	1.11	1.21
2	28.62 28.89	1.4552 1.4690	1.4539 1.4688	1.94	2.09
3	28.69 29.16	1.4586 1.4842	1.4575 1.4830	3.54	3.54
4	26.03 27.00	1.3650 1.3900	1.3651 1.3924	4.02	4.30
5	27.43 28.87	1.4066 1.4678	1.4052 1.4633	8.89	8.47

call them "*red beams*". The spectra of these waves are shown in Fig. 31(b). The resolution of the spectrometer used for these measurements is lower (~ 230 GHz), but its accuracy is better. From the measurements obtained at these wavelengths in the red region of the spectrum we inferred the infrared values of the signal wavelengths given in Table 1. Figure 31(c) shows the second harmonics of the signals (labeled as $\lambda_{s1}/2$ and $\lambda_{s2}/2$) and the sum-frequency (λ_{SFG}) between them. The appearance of the sum-frequency with an intensity higher than that of the second harmonic signals means that the signals overlap well in both space and time. The bandwidth of the sum-frequency signal is ~ 0.4 nm, which at that wavelength corresponds to ~ 230 GHz, which is the resolution of the spectrometer.

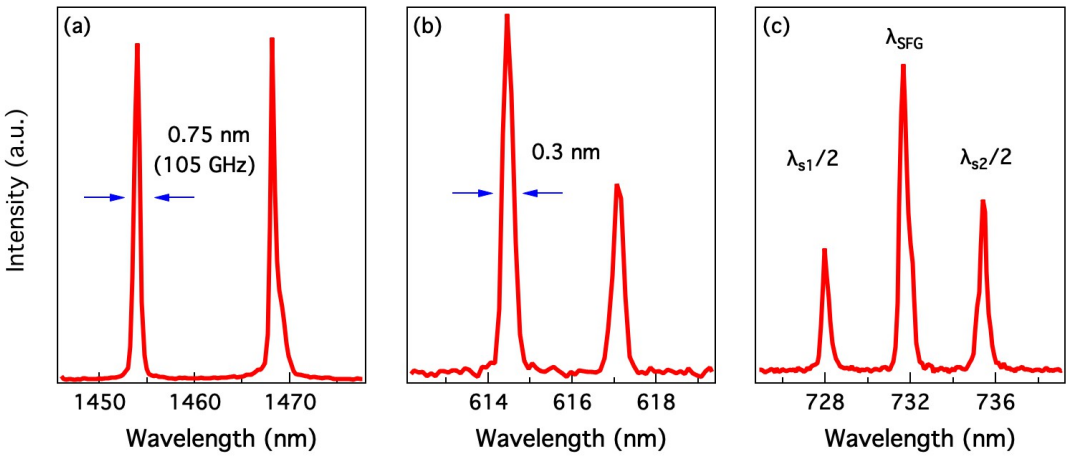

Figure 31. Spectra obtained from Grating #2 using optical parametric oscillation. (a) signals measured in the infrared; (b) sum-frequency between the pump and signals, measured in the visible portion of the spectrum; (c) second harmonic and sum-frequency generation of the pair of signal beams. Data taken at room temperature.

Other data obtained using the OPO are shown in Fig. (32). The figure shows the spectra obtained with Grating #3. Figure 32(a) shows the signals detected using the same infrared spectrometer but with a 400 ln/mm grating. It can be seen in Fig. 32(b) that the "*red beams*", have the same bandwidth ($\sim 230GHz$). Again, from the measurements obtained of these wavelengths in the red region of the spectrum, the infrared wavelengths were inferred and are given in Table 1. Figure 32(c) show the second harmonics of the signals and the sum-frequency peak (λ_{SFG}). As was said before, this peak means that the generated signals are well overlapped. The bandwidth of λ_{SFG} is $\sim$ 0.4 nm, which corresponds to $\sim$ 230 GHz.

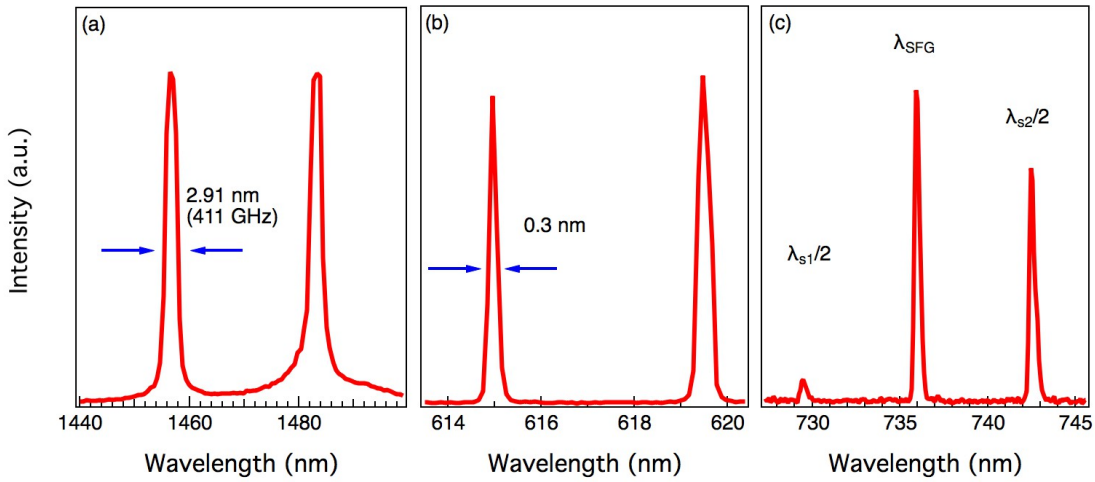

Figure 32. Spectra obtained from Grating #3 using optical parametric oscillation. (a) signals measured in the infrared; (b) sum-frequency between the pump and signals, measured in the visible portion of the spectrum; (c) second harmonic and sum-frequency generation of the pair of signal beams. Data taken at room temperature.

Figure (33) shows the spectra obtained with Grating #1. In this figure we can observe the satellite peaks on each side of the main *red beams*. The satellite peaks are predicted in theory as was explained in Chapter (2). Figure 33 (a) shows the "red beams" and next to each one a satellite peak appears. The satellite peaks are also 1.2 THz away from the main peaks. Figure 33(b) shows the second harmonic of the signals, λ_{s1} and λ_{s2}, and the sum-frequency peaks between them, labeled as λ_{SFG}.

Figure (34) shows the spectra obtained with Grating #4. In this case Fig. 34(a) shows the spectra in the visible region of the spectrum. The first signal generated corresponds to 1365 nm which has low intensity. This is because its corresponding idler is 4822.8 nm and, in this region the absorption is high as can be seen in Fig. 18(b) of Chapter (2). Comparing with the results shown before it can be seen that the

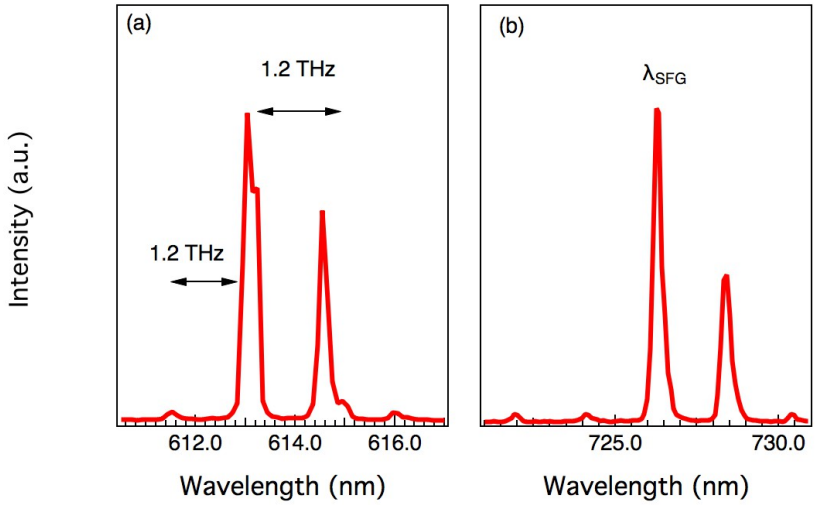

Figure 33. Spectra obtained from Grating #1 using optical parametric oscillation. (a) sum-frequency between the pump and signals, measured in the visible portion of the spectrum; (b) second harmonic and sum-frequency generation of the pair of signal beams. Data taken at room temperature.

λ_{SFG} in Fig. 34(b) is lower. This result was obtained at the beginning of our experiments and this Grating was not used to generate THz radiation because of the high absorption at these wavelengths.

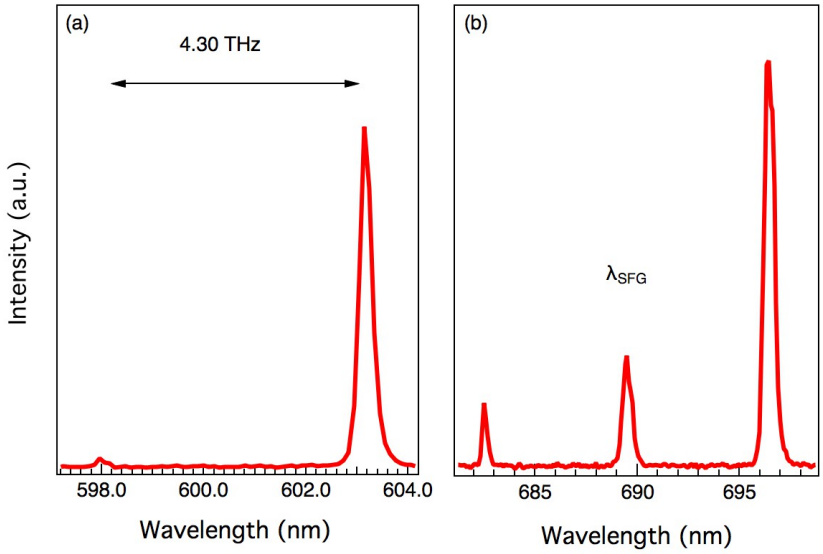

Figure 34. Spectra obtained from Grating #4 using optical parametric oscillation. (a) sum-frequency between the pump and signals, measured in the visible portion of the spectrum; (c) second harmonic and sum-frequency generation of the pair of signal beams. Data taken at room temperature.

The temporal profiles of the pulses are shown in Fig. (35). The data was taken with the OPO operating well above threshold and detected with fast photodiodes (risetime < 175 ps) and a 4 GHz oscilloscope. Figure (35a) shows a comparison of the output pump pulse and the pair of signal pulses combined. The pump and signal pulsewidths are approximately 12 and 5 ns, respectively. Both have large fluctuations, which most likely are due to mode beating. Although the scales for the pump and signals are different, we see that the signals deplete the pump between t~ 2 to and t~7 ns. In order to corroborate that the signal pulses are synchronized, we separated them with a diffraction grating and measured their temporal profiles independently, shown in Fig. (35b). We can see that the pulsewidth of one of the signals is slightly shorter than that of the other, but both pulses are well synchronized, as expected from the results shown in Fig. (31c). The separation between peaks in the signals corresponds to Δt= 0.8 ns, which is, to within experimental error, the round-trip time of the signals in the OPO cavity. For all the grids the temporal profiles are similar, in time duration as well in their synchronization.

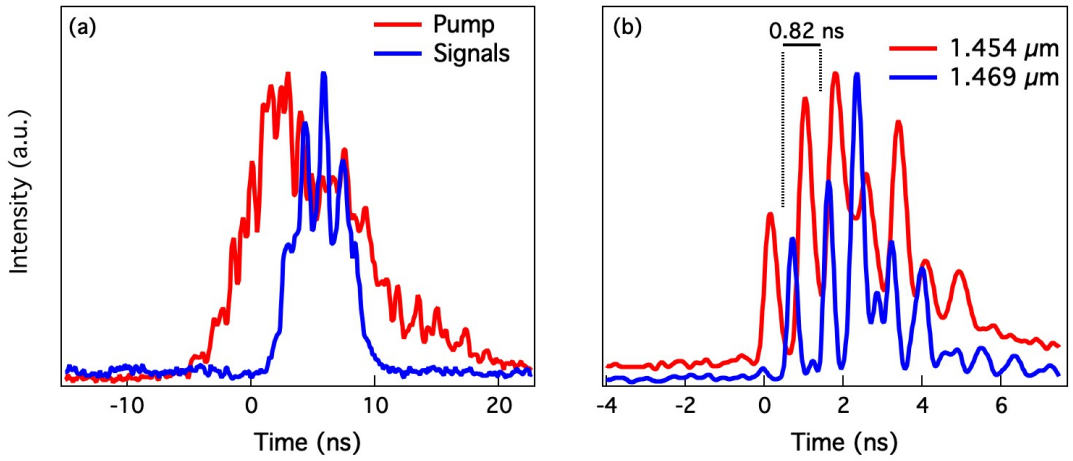

Figure 35. Temporal profile of pump and signal beams obtained with the OPO. (a) Output pump and signals; (b) individual signal beams. Data obtained using Grating 2 pumped well above oscillation threshold.

Figure (36) shows the combined energy of the pair of signal pulses vs incident pump energy in the OPO configuration. The oscillation threshold is around 4 mJ and the output has an approximately linear response above threshold, with a slope efficiency of ~ 10%. At the maximum energy reported in the graph, 740 μJ, the peak power of these pulses is around 150 kW.

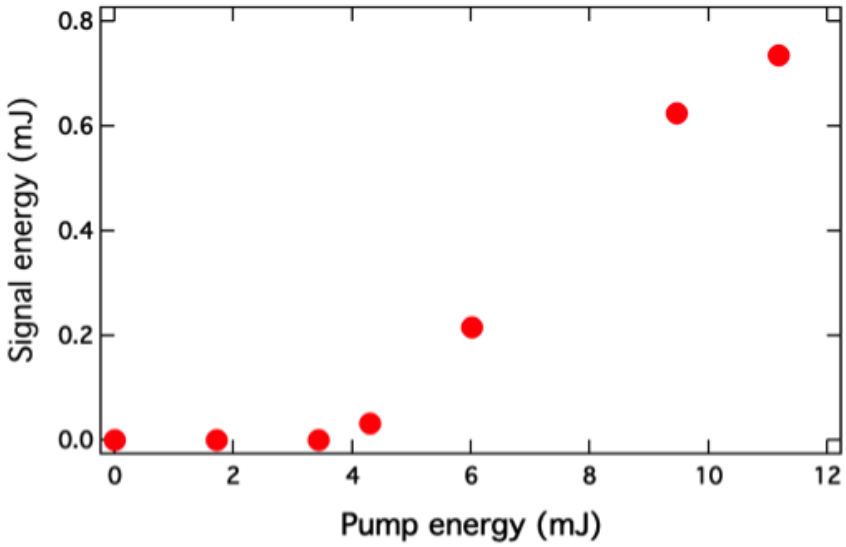

Figure 36. Output energy of the signals vs pump energy in the OPO configuration.

5.1.1 Terahertz generation using OPO source

Figure (37) depicts the experimental set-up for THz generation and detection. A dichroic beamsplitter is placed at the output of the OPO; it reflects wavelength below ~ 1300 nm separating the remnant pump from the signal and idler waves generated in the crystal. It also reflects the "red beams", produced by the non-phase-matched sum-frequency generation between the pump and signal beams as well as the second harmonics of the signal waves and their sum. A lens L_3 (f= 100 mm) was used to collimate the diverging beams in order to confine them in the organic crystal, the diameter of the incident signal beams was ~ 1 mm, the FWHM duration of the pair of signal pulses was 5 ns, and their maximum combined energy was 740 μJ, so the instantaneous irradiance was ~ 4.7 MW/cm^2. The transmitted signal and idler waves go through a high-pass filter (Thorlabs filter FEL 1300) which rejects the idler waves and the remaining signal waves are incident on the organic HMQ-TMS crystal. It is a 0.46 mm thick trapezoidally-shaped plate, prepared by a cleaving method (Jeon *et al.*, 2013); it has an area of ~ 16 mm^2, with its polar axis parallel to the plate's surfaces. A 1-mm thick slab of black HDPE (high density polyethylene) blocks the signal waves that emerge from the HMQ-TMS crystal, transmitting only the THz signal, which is sensed by a pyroelectric detector. The pyroelectric detector is based on lithium tantalate with 3 mm^2 of active area and the spectral region of detection has a range from THz to visible (Sciencetech SCI420BJ-0). According to its specifications, the peak voltage response

of this detector is 1mV per 1 nJ of incident energy, calibrated from $\lambda = 100$ nm − 1 mm. We verified this calibration at 1.047 μm with our home-made laser using another calibrated detector; we assume that the calibration extends into the frequencies we generated. The detection of the THz signal was triggered by the detection of the 1.064 μm pulse reflected by the first dichroic filter. In order to reduce background noise, a few baffles were placed in the set-up (not shown in Fig. (37)) to block spurious reflections of the signals and pump beams; these baffles also blocked air currents that created noise in the pyroelectric detector. A beam-splitter separates the 1.064 μm pulse from the "*red beams*", the second harmonics of the signal beams and their sum (λ_{SFG}). These in turn were detected with visible spectrometer (Ocean Optics HR4000) with a resolution of ∼ 100 GHz. By measuring the wavelength of the "red beams" the wavelength of the signals could be determined as explained before, in this section only these spectra are shown. Since we simultaneously recorded the spectra of the sum-frequency generation of the signals (λ_{SFG}), we could determine if the signal beams were synchronized or not. Whenever they were not, we did not get a signal from the pyroelectric detector, even though both signal beams were present. This is a clear indication that what we measured was THz radiation produced by DFG and not leakage of the signal or pump beams through the HDPE filter.

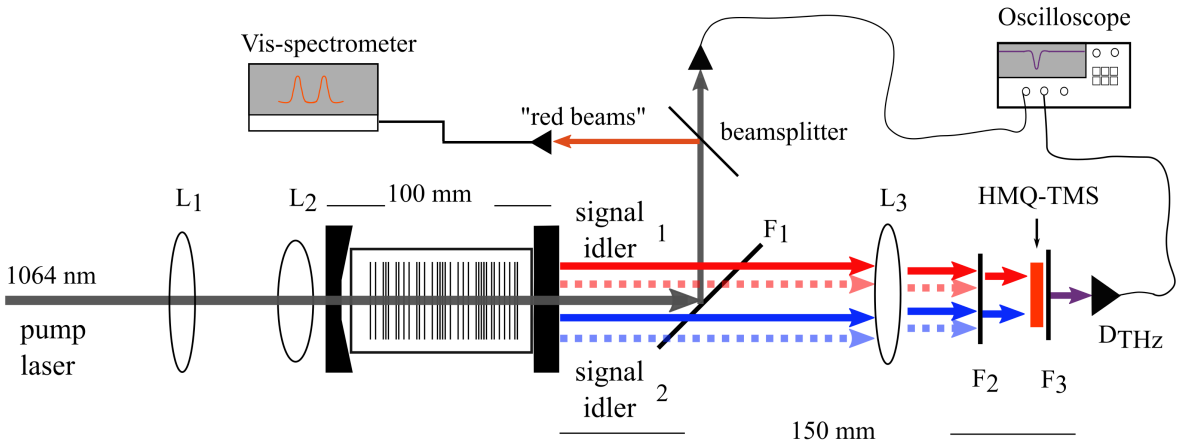

Figure 37. Experimental set-up for THz detection using the OPO system.

The THz generation and the spectra of Gratings #1, #2 and #4, according to Table 1, are shown in Figs. (38)-(40). In each figure, the spectrum obtained in the visible region is shown. It is important to note that the peak of the sum of frequencies (λ_{SFG}) always appears as a sign that the signals are synchronized and overlapped, which is a requirement to obtain THz by DFG. Table 2 shows the results obtained only with three

different grids. The other grids were damage in other experiments and could not be used to obtain THz pulses using OPO as source. In the next section corresponding to THz generation using OPG we obtain THz pulses for all the grids, from 1.43 to 10 THz.

Table 2. THz radiation generated by DFG between different pairs of signals using OPO.

Signals λ (μm)	DFG Frequency (THz)	Signal pair energy (μJ)	THz energy (nJ)	Energy conversion efficiency (%)
1.4480 and 1.4565	1.21	740	47	0.0062
1.4539 and 1.4688	2.09	500	25	0.0033
1.4577 and 1.4830	3.54	500	16	0.0048

Figure (38) shows the results of the generation and detection of 1.21 THz pulses. In Fig. (38 a) the "*red beams*" are shown and Fig. (38 b) shows the second harmonics of the signals as well as their sum (λ_{SFG}). Signals energy was set from 0 to 740 μJ, Fig. (38 c) shows the response of the pyroelectric detector seen on the oscilloscope at different signals energy. The THz pulses energy obtained varies from ~ 10-46 nJ. The maximum efficiency in this case was 0.0062%.

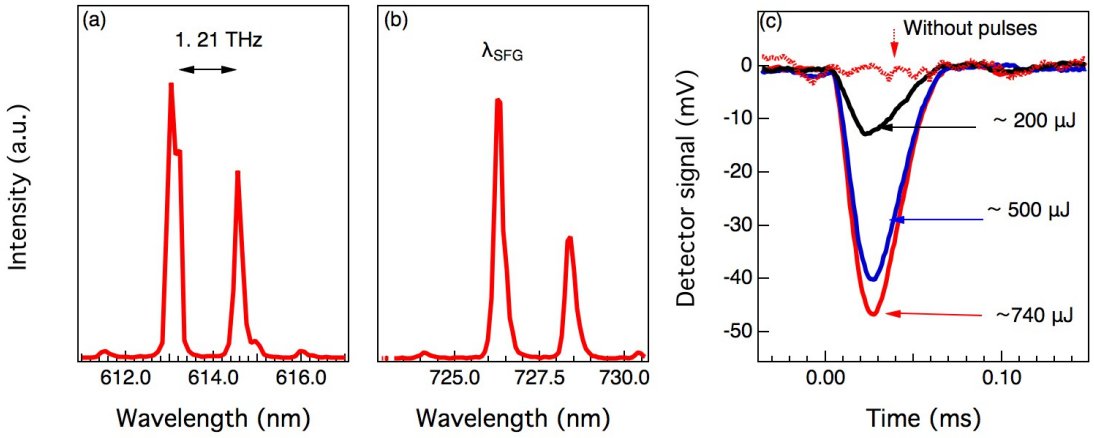

Figure 38. THz generation and detection. a) “Red beams” detected with a visible spectrometer; the satellites also appear; b) second harmonics and sum-frequency of the signals; here the satellites barely appear; c) response of the pyroelectric detector to the THz signals. The polarizations of the signal beams are aligned with the polar axis the HMQ-TMS sample.

Figure (39) shows the results of the generation and detection of 2.09 THz pulses. Signals energy was set from 0 to 740 μJ and the maximum pyroelectric response seen on the oscilloscope corresponds to ~ 25 nJ which is shown in the figure. The efficiency in this case was 0.0033%.

Figure (40) shows the results of the generation and detection of 3.54 THz pulses. The energy of the signals was set from to 350 μJ and at the maximum pyroelectric

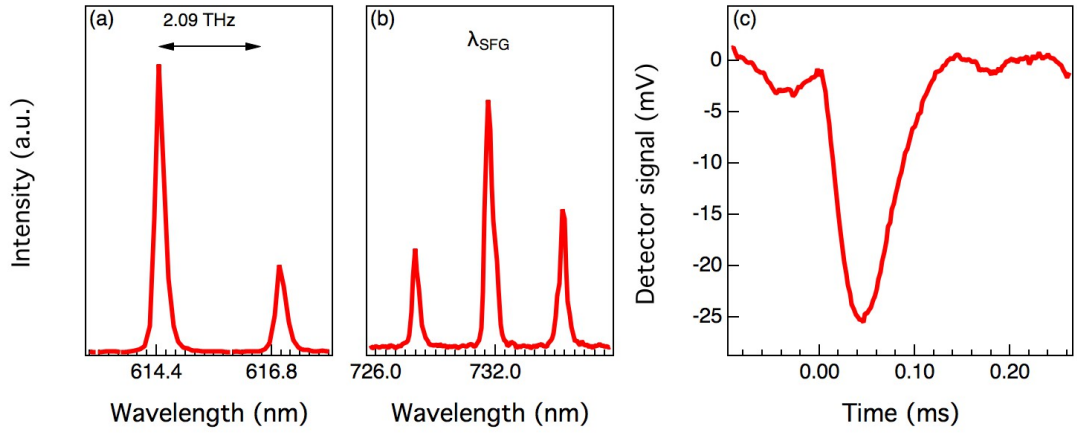

Figure 39. THz generation and detection. from Grating #2 using OPO pumping. In (a) "red beams" spectra as a result of the sum-frequency between pump and signals at different intensities, (b) second harmonic and sum-frequency generation of the pair of signal beams and, (c) 1.93 THz radiation detected at the highest energy.

response seen on the oscilloscope corresponds to ∼ 17 nJ. In this case the efficiency was 0.0048 %.

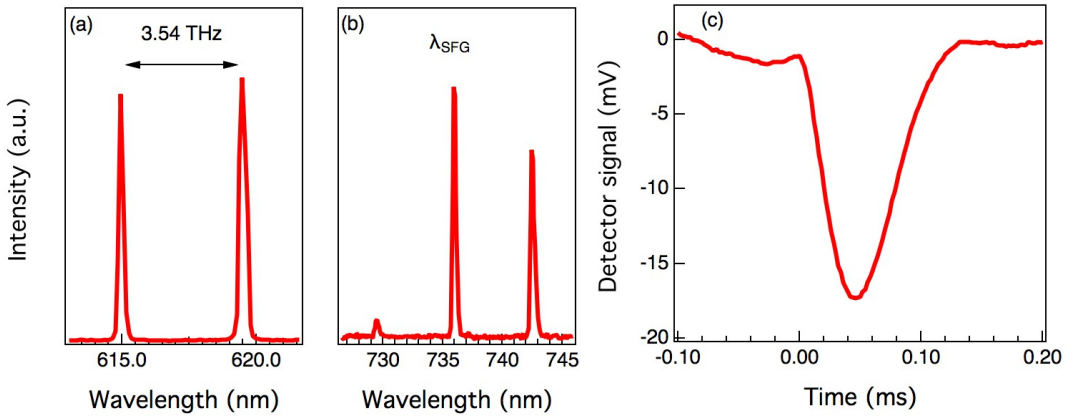

Figure 40. THz generation from Grating #4 using OPO pumping. In (a) "red beams" spectra as a result of the sum-frequency between pump and signals at different intensities, (b) second harmonic and sum-frequency generation of the pair of signal beams and, (c) 3.55 THz radiation detected at the highest energy.

Finally, Fig. (41) shows the energy obtained at different THz frequencies, plotted in red. Note that only three gratings were used because some of them were damaged by other experiments done previously. According to the optical properties of the crystal presented in Chap.(5), the maximum conversion efficiency that can be obtained is limited by the ratio of the pump to THz photon energies, which varies from 0.6% for 1.2 THz to 4.5% for 10 THz; this means that the conversion efficiencies in this configuration is less than 10%. The efficiency in percentage is plotted in blue.

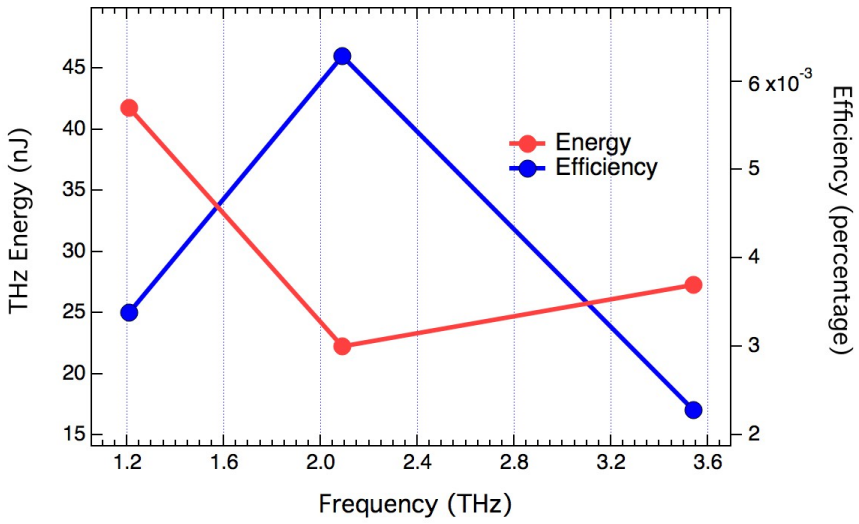

Figure 41. Energy obtained at different THz frequencies.

5.2 Optical parametric generation design

In another experiment, we used a short-pulse (∼1.6 ns FWHM pulsewidth) passively Q-switched laser as the pump. Since the length of the pulse is comparable to the optical path length of the 50 mm long APLN sample, a resonant cavity does not substantially improve the energy of the pulses nor does it reduce their bandwidth, so it was not used; optical parametric generation was sufficient. The pump was a home-built diode-pumped Nd:YLF laser. A fiber-coupled (NA=0.22, 200 μm core diameter) pulsed diode laser is focused to a diameter of roughly 1 mm on an a-cut Nd:YLF crystal (3 x 3 x 12 mm). The pump diode has a nominal CW output power of 30 W; after coupling into and out of the fiber and after traversing the collimating and focusing lenses, the peak power incident on the YLF crystal is approximately 16 W when the diode is operated in a pulsed mode (2 ms pulsewidth). A Cr:YAG crystal with an initial transmittance of 60% is used as the saturable absorber. The Nd:YLF and Cr:YAG crystals are placed in a metal block to extract the heat. The cavity consists of curved input mirror (*radius of curvature= 500 mm*) and flat output coupler, separated by 35 mm; the input mirror is highly reflective at 1047 nm and highly transmitting at 808 nm, while the output coupler mirror has a reflectivity of 70% at 1047 nm. This laser emits well-polarized 1047 nm pulses with pulsewidths of ∼ 1.6 ns FWHM; the energy per pulse is ≈ 350 μJ at a repetition rate of 27 Hz. The M^2 of the beam is ∼ 3. This laser is very similar to the one described in (Cudney and Minor, 2018); the main differences are the power of the diode laser used to pump the Nd:YLF sample and the initial transmittance of the

saturable absorber.

The experimental set-up used to obtain pairs of pulses by OPG is shown in Fig (42). In this case only one spherical lens (f=*75 mm*) is used to focus the pulses onto the APLN sample. The beam waist inside the 50 mm long crystal was estimated to have a FWHM of ∼ 120 μm, so at 350 μJ per pulse the fluence is ∼*3* J/cm^2, which is at the border of the damage threshold. The FWHM of the pump beam at the entrance and exit planes of the crystal was estimated to be ∼ 190 μm.

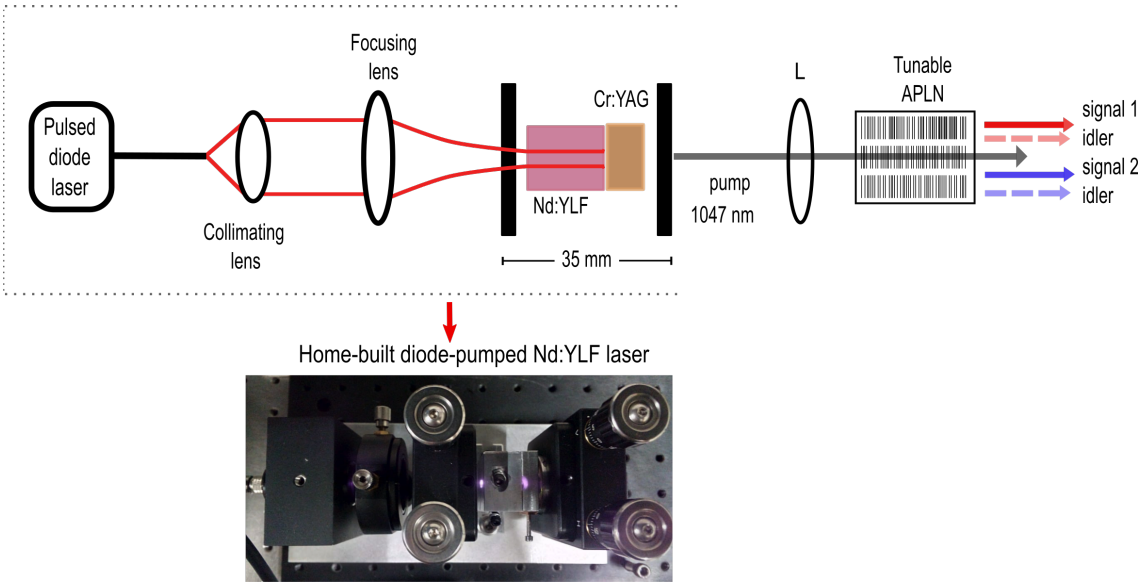

Figure 42. Experimental set-up for optical parametric generation.

The OPG experiments were performed with the same APLN sample that the one used in OPO configuration. However, since the pump wavelength is slightly different, the expected wavelengths and frequency differences are not the same as those of the OPO experiments. These values as well as the experimental values are shown in Table 3.

Figure (43) shows the data obtained with Grating #2, the same one used to obtain the OPO data shown in Figs. (31) and (35). Figure (43 a) shows the spectra of the signals in the infrared. The bandwidth is larger (∼ 175 GHz) than what was obtained with the OPO configuration shown in Figs. (31). This is to be expected, since the feedback of the cavity and the longer pump pulse duration narrows the bandwidth of the OPO output. Figure (43 b) shows the spectra of the sum-frequency generation between the pump and the signals, which is also slightly broadened (∼ 0.4 nm). Figure (43 c) shows the second harmonics of the signals and the sum between them. The peak

Table 3. Parameters of the APLN sample used in the OPG configuration.

Grating	Period (μm)	Signals λ (μm) theory	Signals λ (μm) experiment	$\Delta\nu$ (THz) theory	$\Delta\nu$ (THz) experiment
1	28.51 28.67	1.4348 1.4436	1.4333 1.4435	1.127	1.43
2	28.62 28.89	1.4408 1.4566	1.4380 1.4547	2.26	2.29
3	28.69 29.16	1.4390 1.4550	1.4380 1.4546	2.30	2.39
4	28.69 29.16	1.4575 1.4830	1.4446 1.4744	4.19	4.32
5	27.43 28.87	1.3990 1.4400	1.3960 1.4404	6.25	6.61
6	27.43 28.87	1.3870 1.4554	1.3859 1.4534	10.16	10.05

corresponding to the sum between the two signals is larger than the second harmonic peaks, which means that the pulses are well synchronized, and the bandwidth of the sum-frequency signal is also ∼ 230 GHz, limited by the spectrometer resolution.

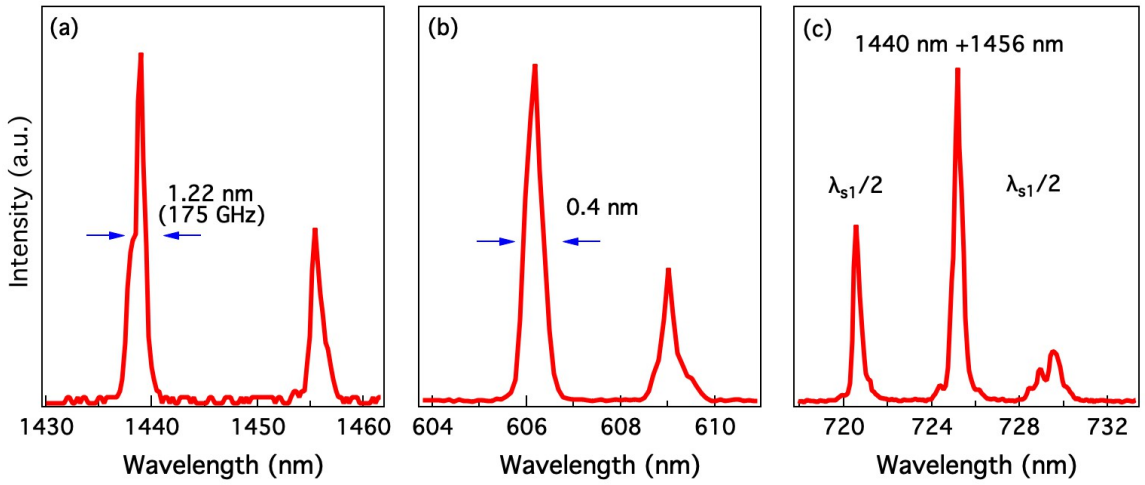

Figure 43. Spectra obtained from Grating #2 using optical parametric generation. (a) signals measured in the infrared; (b) sum-frequency between the pump and signals, measured in the visible portion of the spectrum; (c) second harmonic and sum-frequency generation from the pair of signal beams. Data taken at room temperature.

Figure (44) shows the data obtained with Grating #3. In Fig. (44 a) shows the spectra of the signals in the infrared, in this figure we can observe the satellite peaks on each side of the main peaks. The satellite peaks are also 2.39 THz away from the main peaks. The bandwidth of the signals in the infrared spectra appears to be larger compared with the obtained with Grating #2, this is because it is intentionally saturated in order to appreciate the peaks of the extra signals. Figure (44 b) shows the

"*red beams*" and next to each side the satellite peaks. Figure (44 c) shows the second harmonics of the signals and the sum between them, labeled as λ_{SFG}. Again, the peak corresponding to the sum between the two signals is larger than the second harmonic peaks, which means that the pulses are well synchronized, and the bandwidth of the sum-frequency signal is also ∼ 230 GHz, limited by the spectrometer resolution. The sum-frequency peaks of the extra signals barely appears.

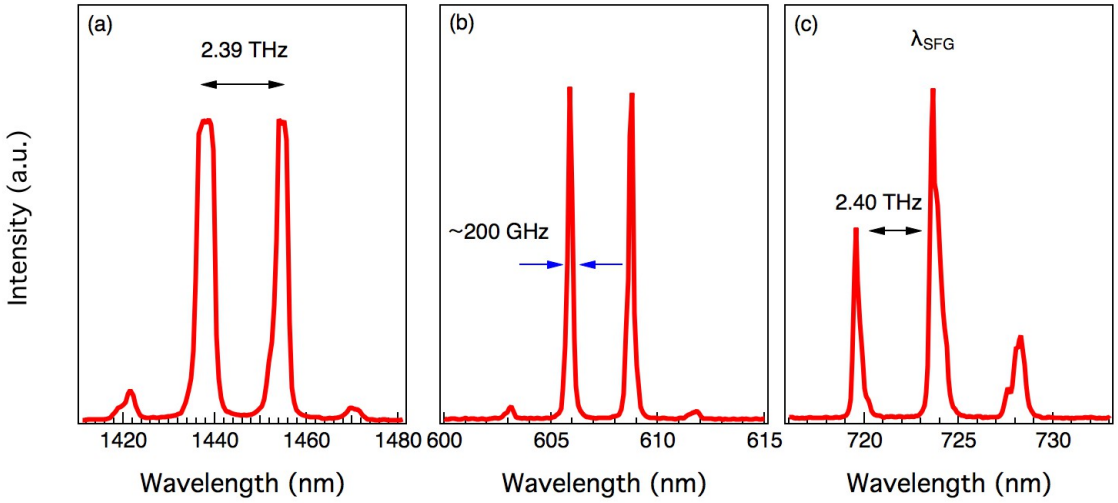

Figure 44. Extra signals appearance from Grating #3 using optical parametric generation. (a) signals measured in the infrared; (b) sum-frequency between the pump and signals, measured in the visible portion of the spectrum; the satellites also appear; (c) second harmonic and sum-frequency generation from the pair of signal beams. Data taken at room temperature.

Figure (45) shows the data obtained with Grating #4. Figure (45 a) shows the spectra of the signals in the infrared. The bandwidth is larger (∼ 317 GHz) than what was obtained with Grating #2. Figure (45 b) shows the spectra of the "red beams", which again is slightly broadened (∼ 0.4 nm). Figure (45 c) shows the second harmonics of the signals and the sum between them. Again, the peak corresponding to the sum between the two signals is larger than the second harmonic peaks, which means that the pulses are well synchronized, and the bandwidth of the sum-frequency signal is ∼ 220 GHz, limited by the spectrometer resolution.

Figure (46) shows the temporal profiles of the output pump and the combined signals, taken with a pump pulse of 350 μJ and 1.6 ns pulsewidth. Figure (46 a) shows the output pump and the combined signals. The generated signals have a combined pulsewidth of 0.8 ns and a combined energy of 38 μJ, which gives a peak power of ∼ 47 kW. Figure (46 b) shows the profiles of the signals separated with a diffraction grating;

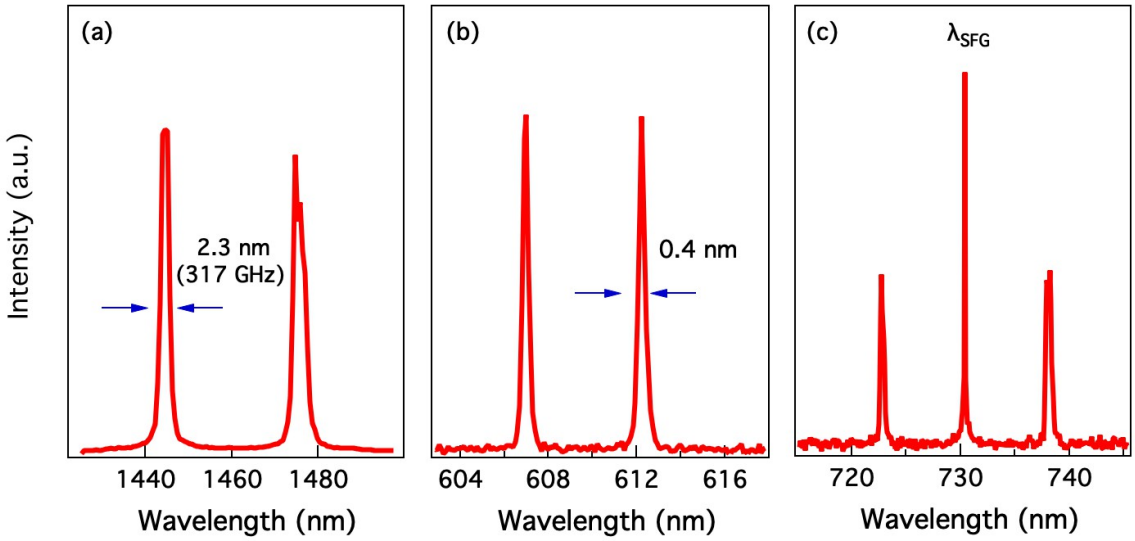

Figure 45. Spectra obtained from Grating #4 using optical parametric generation. (a) signals measured in the infrared; (b) sum-frequency between the pump and signals, measured in the visible portion of the spectrum; (c) second harmonic and sum-frequency generation from the pair of signal beams. Data taken at room temperature.

the signals are very well synchronized among themselves.

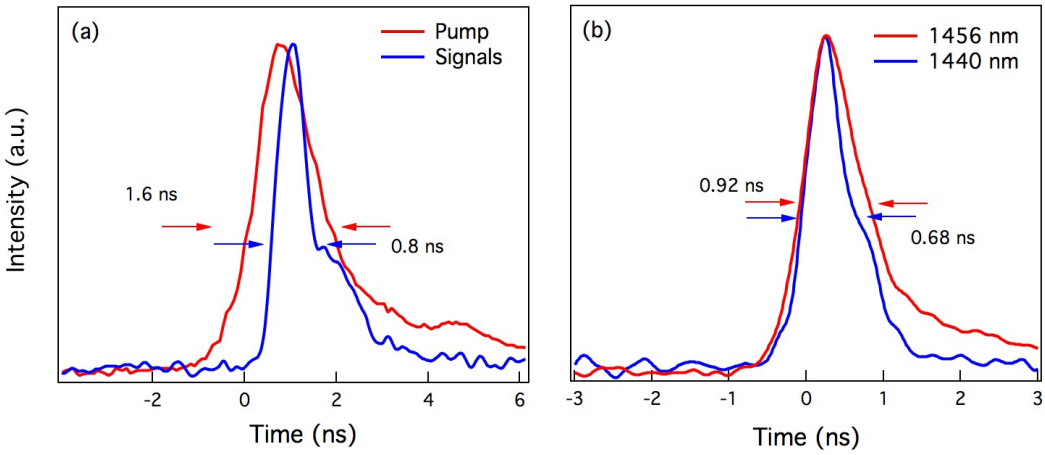

Figure 46. Temporal profiles of the output pump and signals obtained with OPG. (a) Output pump and combined signals; (b) individual signal beams. Data obtained using Grating #2.

In the OPG experiments the combined peak power was lower, ~ 47 kW, is sufficient to obtain THz radiation. The advantages of this system are mainly the simplicity, low cost and compactness of the system as well as the higher repetition rate.

5.2.1 Terahertz generation using as pump the optical parametric generation

The experimental set-up for THz generation and detection using OPG configuration is shown in Fig. (47). It is similar to the OPO experimental set-up, the main difference is

that there is no need to focus the signals in the organic crystal since the signals output beam diameter is ~ 1 mm. The distance from the output signal to the HMQ-TMS crystal is 100 mm. The combined energy of the signals was 20-38 μJ, depending on which pair of signals was used, so the instantaneous irradiance was between ~ 0.75 and 1.4 MW/cm^2. The crystal was mounted on a rotation stage to observe the dependence of the energy of the THz signal on its orientation with respect to the polarization of the signal beams. Care was taken to ensure that the signal being detected was actually THz radiation produced by the organic crystal. As was made in OPO configuration, in order to reduce background noise, a few baffles were placed in the set-up (not shown in Fig. (47)) to block spurious reflections of the signals and pump beams; these baffles also blocked air currents that created noise in the pyroelectric detector. Since we simultaneously recorded the spectra of the sum-frequency generation (λ_{SFG}) of the signals, we could determine if the signal beams were synchronized or not. Whenever they were not, we did not get a signal from the pyroelectric detector, even though both signal beams were present. This is a clear indication that what we measured was THz radiation produced by DFG and not leakage of the signal or pump beams through the HDPE filter.

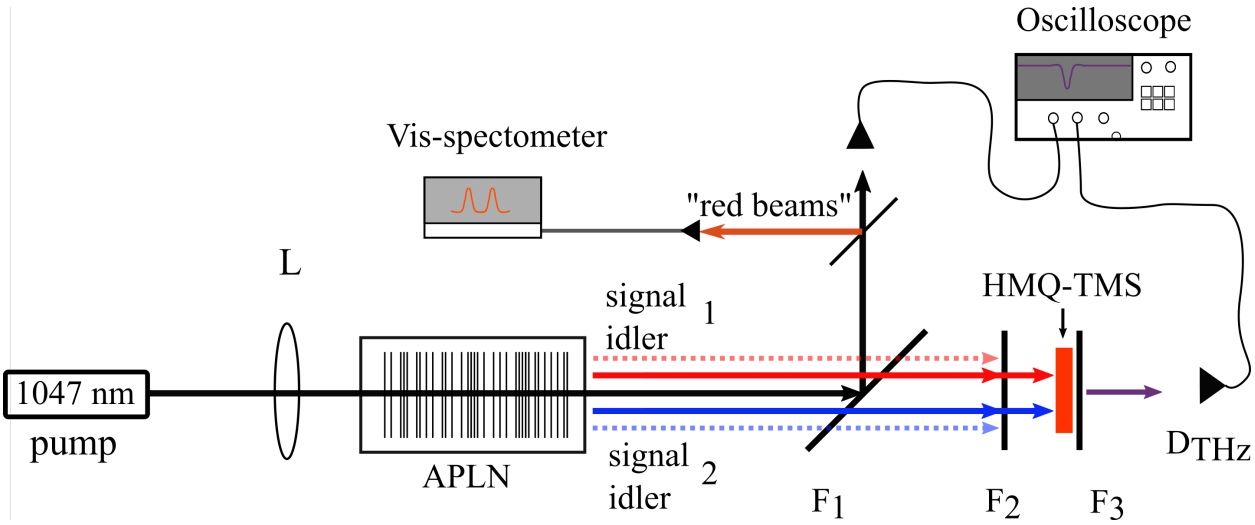

Figure 47. Experimental set up for THz detection in the OPG system.

In Table 4 is summarized the results obtained with the four gratings used for THz generation and the energy efficiency conversion for each one.

Figure (48) shows the results of the generation and detection of 1.43 THz pulses. Figure (48 a) shows the spectra of the "*red beams*" and in Fig. (48 b) shows the peaks

Table 4. THz radiation generated by DFG between different pairs of signals.

Signals λ (μm)	DFG Frequency (THz)	Signal pair energy (μJ)	THz energy (nJ)	Energy conversion efficiency (%)
1.4335 and 1.4433	1.43	35	32	0.091
1.4380 and 1.4547	2.39	38	40	0.105
1.3960 and 1.4404	6.61	30	30	0.100
1.3859 and 1.4534	10.05	20	15	0.075

corresponding to the second harmonic generation of the signals but, most importantly, the λ_{SFG} peak. Figure (48 c) shows the pyroelectric response seen on the oscilloscope, which corresponds to 32 nJ. In this case, the signals input energy is 35 μJ, then the efficiency corresponds to 0.091%. In OPG configuration we cannot vary the signals energy, but we rotate the organic crystal to change the direction of the polarization of the signal beams with respect to the crystal's polar axis: the maximum occurred when the beams were polarized parallel to the polar axis and zero when its rotated by 90°, as expected (Jazbinsek *et al.*, 2019).

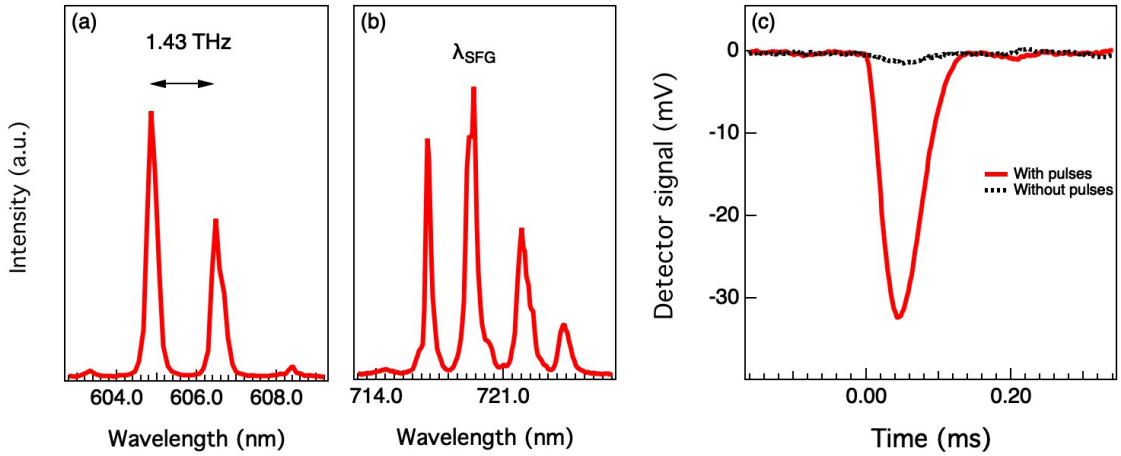

Figure 48. 1.43 THz generation and detection. a) "Red beams" detected with a visible spectrometer; the satellites also appear; b) second harmonics and sum-frequency of the signals; here the satellites barely appear; c) response of the pyroelectric detector to the THz signal. The polarizations of the signal beams are aligned with the polar axis of the HMQ-TMS sample.

Figure (44) shows the results of the generation and detection of 2.39 THz pulses. In Figs. (49 a) and (b) the "*red beams*" spectra is shown and, Fig. (49 c) shows the pyroelectric response seen on the oscilloscope. In this case, the combined signals energy is 38 μJ and the THz pulse energy detected corresponds to 40 nJ and, the efficiency is 0.105%.

Figure (50) shows the results of the generation and detection of 6.61 THz pulses.

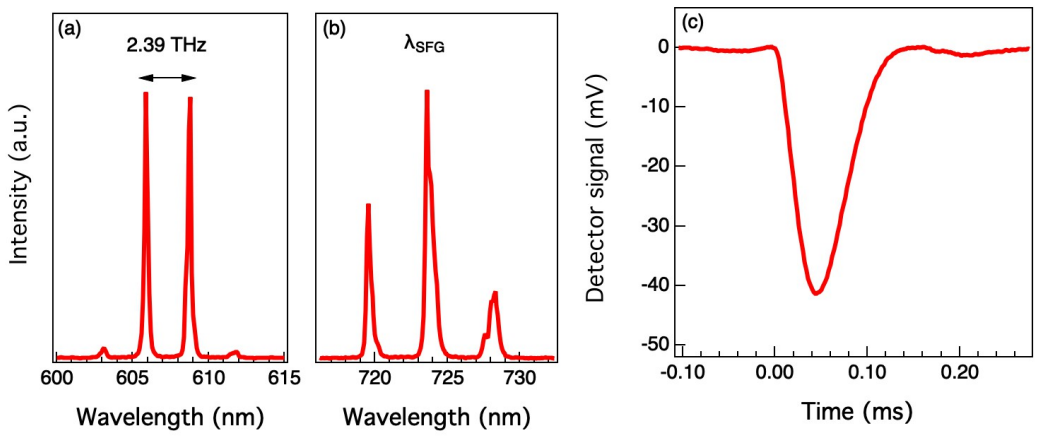

Figure 49. 2.39 THz generation and detection. a) “Red beams” detected with a visible spectrometer; the satellites also appear; c) second harmonics and sum-frequency of the signals; here the satellites barely appear; d) response of the pyroelectric detector to the THz signal.

Figures (50 a) and (b) show the corresponding spectra and the THz detection is shown in (50 c). In this case, the combined signals energy is 30 μJ and the THz pulse energy detected corresponds to 30 nJ and, the efficiency is 0.100%.

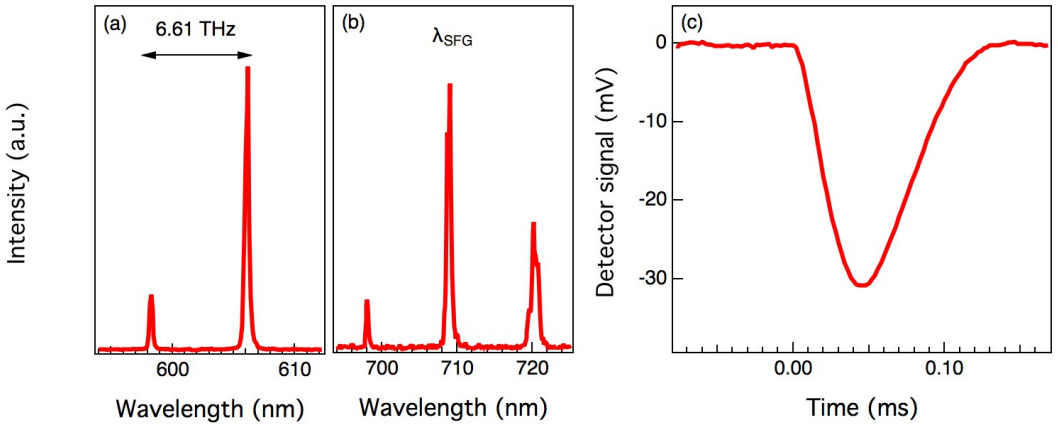

Figure 50. 6.61 THz generation and detection. a) “Red beams” detected with a visible spectrometer; b) second harmonics and sum-frequency of the signals; c) response of the pyroelectric detector to the THz signal.

Figure (51) shows the results of the generation and detection of 10.05 THz pulses. Figures (51 a) and (b) show the corresponding spectra and the THz detection is shown in (51 c). In this case, the combined signals energy is 20 μJ and the THz pulse energy detected corresponds to 15 nJ and, the efficiency is 0.075%.

We also measured the pulse-to-pulse stability of the THz signal. The main source of instability is the pulse-to-pulse variation of energy of the 1.047 μm laser pump pulses,

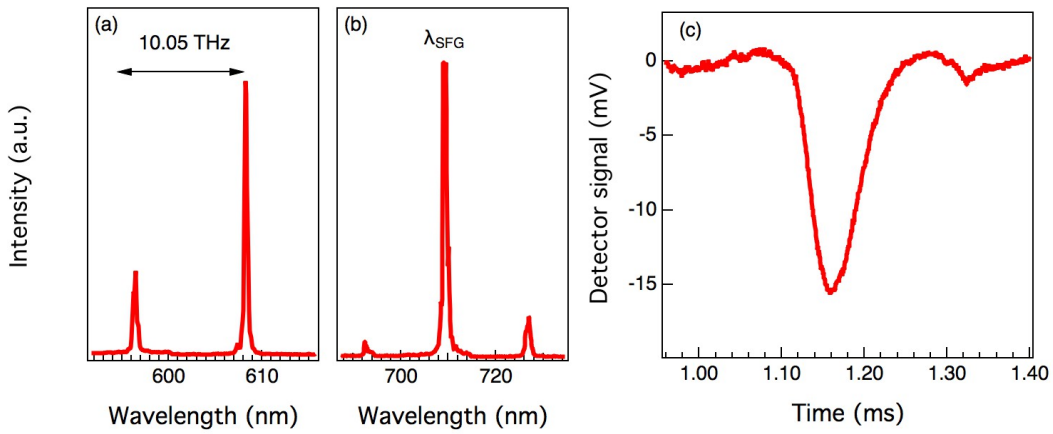

Figure 51. 10.05 THz generation and detection. a) "Red beams" detected with a visible spectrometer; b) second harmonics and sum-frequency of the signals; here the satellites barely appear; c) response of the pyroelectric detector to the THz signals.

which is low (<1%), which creates a variation of the signal pulses. Figure (52 a) shows a histogram of the combined energy of the signal pulses obtained using the same grating used in Fig. (44), $\Delta\nu$ = 2.39 THz; the peak is at 22.2 μJ, with a spread of about ±0.2 μJ. Figure (52 b) shows ten traces of the 2.39 THz signal and their average. Here the average energy is 38.6 nJ per pulse, with a variation of ∼ ±2 nJ, which corresponds to a pulse-to-pulse fluctuation of ∼ 5%

In all the cases the conversion efficiency (THz energy/signal pair energy) is around 0.1%. The absorption of the pump is negligible; however, for all the THz frequencies reported here the absorption coefficient is ∼ 10 mm^{-1}, which reduces the THz output. The maximum conversion efficiency that can be obtained is limited by the ratio of the pump to THz photon energies, which varies from 0.6% for 1.4 THz to 4.5% for 10 THz; this means that the conversion efficiencies that we report are of the order of 10% of the maximum that is possible to achieve under perfect conditions. The THz energy obtained and the efficiency are shown in Fig. (53).

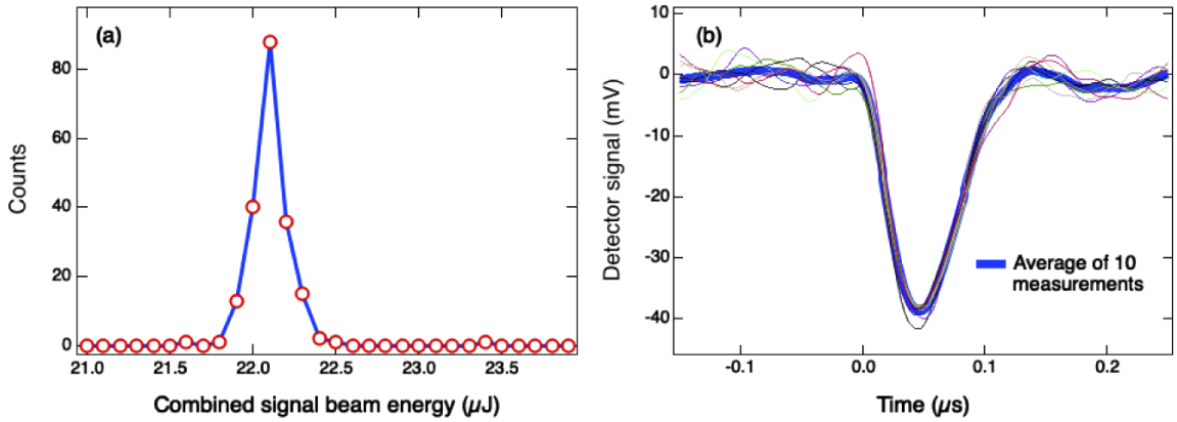

Figure 52. Pulse-to-pulse fluctuations. a) Histogram of the combined energies of 200 signal pulses; b) oscilloscope traces of the THz signal; the thin lines correspond to ten individual traces and the thick blue line corresponds to their average.

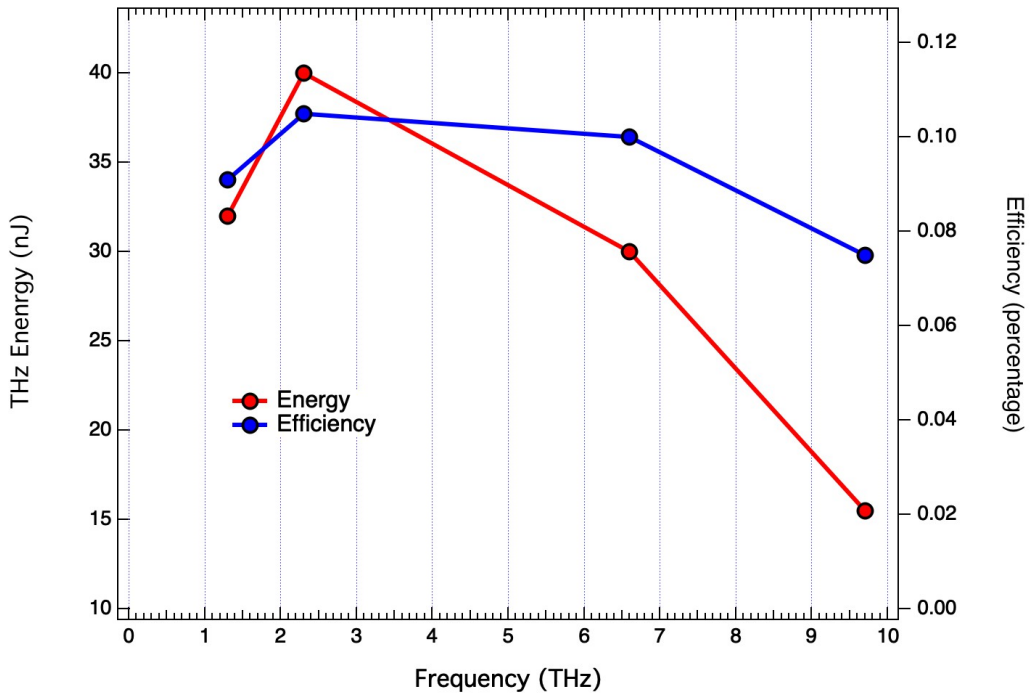

Figure 53. Energy and conversion efficiency obtained at different frequencies.

Chapter 6. Conclusions

We have presented two sources of synchronized pulses based on OPO and OPG that use an aperiodically poled lithium niobate crystal as the nonlinear medium. The bandwidth of the signals, < 105 GHz for OPO and < 175 GHz for OPG, is low due to the use of a long (50 mm) aperiodic structure. In the OPO experiments, we obtained 5 ns signal pulses with a combined energy of 740 μJ; the peak power of these pulses, ~ 50 kW, sufficient to generate usable THz radiation through difference- frequency generation in various nonlinear media. The cavity mirrors used in these experiments were mirrors available in the laboratory; the peak intensity of the pulse pair can be increased by using optimal mirrors for the cavity (high reflectance at the idler wavelengths and low reflectance at the signal wavelengths) as well as using a pump that emits shorter pulses. In the OPG experiments, the combined peak power was lower, ~ 47 kW, which should be sufficient to obtain THz radiation. The advantages of this system are mainly the simplicity, low cost, and compactness of the system as well as the higher repetition rate. In this configuration the pump was focused to a small circular spot, which produces signals with better spatial quality than what is obtained with an elliptically shaped pump. However, a larger signal peak power would be desired. The energy of the signal pulses can be greatly increased by using more energetic pump pulses; however, optical damage of the APLN sample limits the fluence of the pump pulses that can be used, which is already at the damage threshold. The analysis of the aperiodic structure predicts the appearance of satellite peaks besides of the two main peaks, which were observed in the spectra of the 1.21 and 2.39 THz gratings, which are the closest signals generated.

Using both configurations OPO and OPG we obtained THz radiation based on DFG in the HMQ-TMS crystal. The measured signal bandwidth was limited by the resolution of the spectrometer; however, considering 200 GHz to be the narrowest bandwidth of the signals in the OPG experiments, we expect the THz signal to also have a bandwidth < 200 GHz. The high instantaneous irradiance, ~ 1 MW/cm^2, was enough to produce THz radiation with a conversion efficiency of the order of 0.1%. Although the main advantage of this source is its simplicity and low cost, the energy per pulse is comparable to other systems that are far more complex and bulky. For comparison, the system described in (Liu *et al.*, 2014) that is based on DSTMS produces close to 100 nJ per

pulse, which is more than twice what is presented here, but the signal pulses required to obtain the THz pulses are far more energetic, over 2.5 mJ, whereas our system only requires around 40 μJ. The bandwidth of the THz pulses emitted by our system is limited by the bandwidth of the signal beams. This can be reduced by different means, such as using a longer APLN crystal or by injection-seeding with an external CW laser. If this seeding laser were tunable, then we could also achieve tunable narrowband THz radiation. The lowest bandwidth that could be obtained is limited by the pulsewidth, which is close to 0.5 ns (considering that the signal pulses have a pulsewidth of ~0.8 ns), so the lowest achievable bandwidth with this system is of the order of 2 GHz. The OPO system is a more robust system, it also requires that the output beams be collimated to improve the spatial profile before reaching the HMQ-TMS crystal to generate the THz pulses. Since in the OPO the pulses are longer, in this system the THz efficiency is lower compared to the OPG.

Bibliography

Abraham, E., Younus, A., Delagnes, J. C., and Mounaix, P. (2010). Non-invasive investigation of art paintings by terahertz imaging. *Applied Physics A: Materials Science and Processing*, **100**(3): 585–590.

Armstrong, J. A., Bloembergen, N., Ducuing, J., and Pershan, P. S. (1962). Interactions between light waves in a nonlinear dielectric. *Physical Review*, **127**: 1918–1939.

Browell, E. (1989). Differential absorption lidar sensing of ozone. *Procedings in the IEEE*, **77**(3): 419–432.

Browell, E. V., Wilkerson, T. D., and Mcilrath, T. J. (1979). Water vapor differential absorption LIDAR development and evaluation. *Applied Optics*, **18**(20): 3474–3483.

Brundermann, E., Hubers, H., and FitzGerald, M. (2012). *Terahertz Techniques*. Springer.

Brunner, F., Lee, S., Kwon, O. P., and Feurer, T. (2014). THz generation by optical rectification of near-infrared laser pulses in the organic nonlinear optical crystal HMQ-TMS. *Optical material express*, **4**(8): 1586–1592.

Carrillo-Fuentes, M. and Cudney, R. S. (2019). Production of pairs of synchronized pulses by optical parametric generation and oscillation using aperiodically poled lithium niobate. *Applied Optics*, **58**(21): 5764–5769.

Carrillo-Fuentes, M., Cudney, R. S., Lee, S.-H., and Kwon, O.-P. (2020). Production of pairs of synchronized pulses by optical parametric generation and oscillation using aperiodically poled lithium niobate. *Optics Express*, **28**(17): 24444–24451.

Cudney, R. S. and Minor, C. E. (2018). Sub-nanosecond, megawatt compact diode-pumped Nd:YLF laser. *Revista Mexicana de Fisica*, **64**(5): 512–518.

Dhillon, S. S., Vitiello, M. S., Linfield, E. H., Davies, A. G., Booske, J., Paoloni, P., Williams, G. P., Castro-Camus, E., Cumming, D., Simoens, F., Escorcia-Carranza, I., Grant, J., Lucyszyn, S., and Michael, B. (2017). The 2017 terahertz science and technology roadmap. *Journal of Physics D: Applied Physics*, **50**(4): 1–50.

Ding, Y. (2014). Progress in terahertz sources based on difference-frequency generation. *Journal of the Optical Society of America B*, **31**(11): 2696–2711.

Dole, H., Lagache, G., Puget, J., Caputi, K. I., Fernandez Conde, N., Le Floch, E., Papovich, C., Perez Gonzalez, P. G., Rieke, G. H., and Blaylock, M. (2006). The cosmic infrared background resolved by spitzer - contributions of mid-infrared galaxies to the far-infrared background. *Astronomy and Astrophysics*, **451**(2): 417–429.

DrDomenico, M. and Wemple, S. H. (1969). Oxygen-octahedra ferroelectrics I. Theory of electro optical and nonlineal optical effects. *Journal of Applied Physics*, **40**: 720–734.

Fejer, M., Magel, G., Jundt, D., and Byer, R. (1992). Quasi-phase-matched second harmonic generation: tuning and tolerances. *IEEE Journal of Quantum Electronics*, **28**: 2631–2654.

Franken, P. A., Hill, A. E., Peters, C. W., and Weinreich, G. (1961). Generation of optical harmonics. *Phys. Rev. Lett.*, **7**: 118–119.

Giordmaine, J. A. and Miller, R. C. (1965). Tunable coherent parametric oscillation in $LiNbO_3$ at optical frequencies. *Physical Review Letters*, **14**: 973–976.

Grant, W. (1991). Differential absorption and raman lidar for water vapor profile measurements: a review. *Optical Engineering*, **30**(1): 40–48.

Jazbinsek, M., Puc, U., Abina, A., and Zidansek, A. (2019). Organic crystals for THz photonics. *Applied Sciences*, **9**(5): 882–923.

Jeon, J., Kang, B., Kim, J., Jazbinsek, M., Lee, S., Baek, I., Yun, H., Kim, J., Lee, Y., Lee, J., Kim, J., Rottermund, F., and Kwon, O. P. (2013). High-power broadband organic THz generator. *Science Reports*, **3**: 2045–2322.

Jundt, D. H. (1997). Temperature-dependent sellmeier equation for the index of refraction, n_e), in congruent lithium niobate. *Optics letters*, **22**: 1553–1555.

Kawase, K., Hatanaka, T., Takahashi, H., Nakamura, K., Taniuchi, T., and Ito, H. (2000). Tunable terahertz-wave generation from DAST crystal by dual signal-wave parametric oscillation of periodically poled lithium niobate. *Optical Letters*, **25**: 1714–1716.

Kitaeva, G. (2008). Terahertz generation by means of optical lasers. *Laser Physics Lasers*, **5**(8): 559–576.

Kroll, N. (1963). Parametric amplification in spatially extended media and application to the design of tuneable oscillators at optical frequencies. *Proceedings of the IEEE*, **51**: 110–114.

Lee, Y.-S. (2009). *Principles of Terahertz Science and Technology*. Springer.

Leidinger, M., Fieberg, S., Waasem, N., Kühnemann, F., Buse, K., and Breunig, I. (2015). Comparative study on three highly sensitive absorption measurement techniques characterizing lithium niobate over its entire transparent spectral range. *Optics Express*, **23**: 21690–21705.

Lhuillier, J., Torosyan, G., Theuer, M., Avetisyan, Y., and Beigang, R. (2007). Generation of THz radiation using bulk, periodically and aperiodically poled lithium niobate – Part 2: Experiments. *Applied Physics B*, **86**(2): 197–208.

Liu, P., Xu, D., Li, Y., Zhang, X., Wang, Y., Yao, J., and Wu, Y. (2014). Widely tunable and monochromatic terahertz difference frequency generation with organic crystal dstms. *Europhysics Letters*, **106**(6): 60001.

Majkic, A., Zgonik, M., Petelin, A., Jazbinsek, M., Ruiz, B., Medrano, C., and Gunter, P. (1961). Terahertz source at 9.4 THz based on a dual-wavelength infrared laser and quasi-phase matching in organic crystals OH1. *Applied Physics Letters*, **105**: 141115–141118.

Rieke, G. (2003). *Detection of Light. From the UV to the submillimeter*. Cambridge University Press.

Robles-Agudo, M. and Cudney, R. S. (2011). Multiple wavelength generation using aperiodically poled lithium niobate. *Applied Physics B*, **103**: 99–106.

Seitz, W., Katz, M., Sunney, X., Ganikhanov, F., Carrasco, S., and Kopf, D. (2006). Broadly tunable dual-wavelength light source for coherent anti-stokes raman scattering microscopy. *Optics Letters*, **31**: 1292–1294.

Shen, Y. R. (1984). *Principles of nonlinear optics*. New York: Wiley-Interscience.

Taniuchi, T. and Nakanishi, H. (2004). Collinear phase-matched terahertz-wave generation in GaP crystal using a dual-wavelength optical parametric oscillator. *Journal of Applied Physics*, **95**(12): 7588–7591.

Taniuchi, T., Okada, S., and Nakanishi, H. (2004). Widely tunable terahertz-wave generation in an organic crystal and its spectroscopic application. *Journal of Applied Physics*, **95**(11): 5984–5988.

Vidal, F. and Tadjeddine, A. (2005). Sum-frequency generation spectroscopy of interfaces. *Report on Progress in Physics*, **68**: 1095–1127.

Weis, R. S. and Gaylord, T. K. (1985). Lithium niobate: Summary of physical properties and crystal structure. *Applied physics A: Materials Science Processing*, **37**: 191–203.

Wojde, J. C. and Íñiguez, J. (2014). Ferroelectric transitions at ferroelectric domain walls found from first principles. *Physical Review Letters*, **112**: 247603–247608.

Zhang, X. C., Ma, X. F., Jin, Y., Lu, T. M., Boden, E. P., Phelps, P. D., Stewart, K. R., and Yakymyshyn, C. P. (1992). Terahertz optical rectification from a nonlinear organic crystal. *Applied Physics Letters*, **61**(26): 3080–3082.

Zhao, P., Ragam, S., Ding, Y. J., and Zotova, I. B. (2010). Compact and portable terahertz source by mixing two frequencies generated simultaneously by a single solid-state laser. *Optical Letters*, **35**(23): 3979–3981.

Appendix

For an aperiodically-poled crystal, the effective second-order nonlinearity as a function of the wavevector mismatch parameter for three extraordinary polarized waves in general is given by

$$\chi^{(2)}_{eff}(\Delta k) = \frac{\chi_{33}}{L}\int_0^L g(x) exp[i\Delta k x]dx \tag{72}$$

where $g(x)$ describes the spatial variation of the sign of the nonlinearity ($g(x) \pm 1$) and L is the length of the aperiodic structure. We want to obtain two signal frequencies ω_{s1} and ω_{s2} that are separated by the desired THz frequency $\delta\omega$. Let $k_1 = 2\pi/\Lambda_1$ and $k_1 = 2\pi/\Lambda_2$, where Λ_1 and Λ_1 are the poling periods needed to get ω_{s1} and ω_{s2} by quasi-phase-matching. The aperiodic structure we use is given by

$$g(x) = sign\,[cos(k_1 x) - cos(k_2 x)] = sign\left[sin(\bar{k}x) sin\left(\frac{\delta k}{2}x\right)\right]. \tag{73}$$

Here $\bar{k}$ is the average of k_1 and k_2, that is $\bar{k} = (k_1 + k_2)/2$, and δk. The structure is essentially a periodic structure with a period that has 180° phase shifts every distance D, given by $D = 2\pi/\delta k$, as shown in Fig. (54). If for simplicity we restrict the lengths such that D is an integer multiple of the period Λ and in turn the length L of the crystal is an integer multiple of D, then it can be shown that

$$|\chi^{(2)}_{eff}(\Delta k)| = \chi_{33}\left|\frac{2}{\Delta k L} tan\left(\frac{\Delta k \Lambda}{4}\right) tan\left(\frac{\Delta k D}{2}\right) cos\left(\frac{\Delta k L}{2}\right)\right|. \tag{74}$$

The position of the peaks is governed mainly by the values of Δk where $tan\,(\Delta k/2)$ is

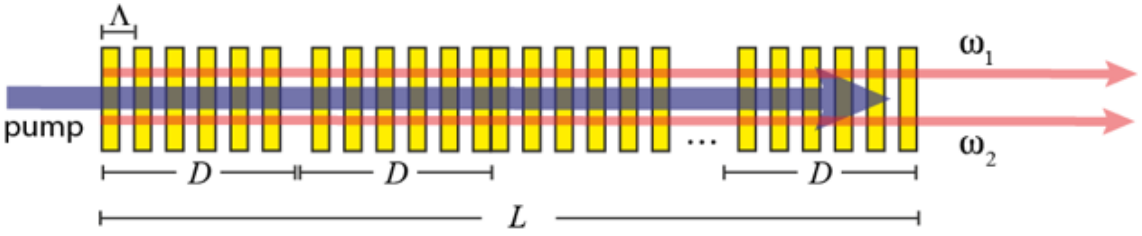

Figure 54. Aperiodic structure

large, that is, when its argument is close to an odd multiple of $\pi/2$, so the peaks occur when

$$\Delta k \sim \frac{\pi}{D}(2q + 1), \tag{75}$$

where q is an integer. The separation between peaks is therefore $2\pi D$.

The magnitude of the effective nonlinearity given in Eq. (74), normalized to χ_{33}, is plotted in Fig. (55). As can be seen, there are two sets of peaks that are essentially mirror images of each other, where the mirror plane is at $\Delta k = 2\pi/\Lambda$, that is, when $q = D/\Lambda$. Each peak is described approximately by the magnitude of a sinc function, centered around the values of Δk given by Eq. (75). On the right hand side of the mirror plane, the first and largest peak occurs at $\Delta k = \pi(2/\Lambda + 1/D)$, with a maximum value of $(2/\pi)^2$; the next peaks decrease to 1/3, 1/5... of this value. The widths are governed by the $cos(\Delta kL/2)$ factor of Eq. (74), and are equal to $2\pi/L$ for all of the peaks. For comparison, Fig. (55) also shows the effective nonlinearity for the case of two consecutive periodically-poled regions, each with a different poling period and length $L/2$. Two peaks appear, but they are shorter ($1/\pi$) and twice as wide ($4\pi/L$), since only half of the crystal contributes appreciably to each peak.

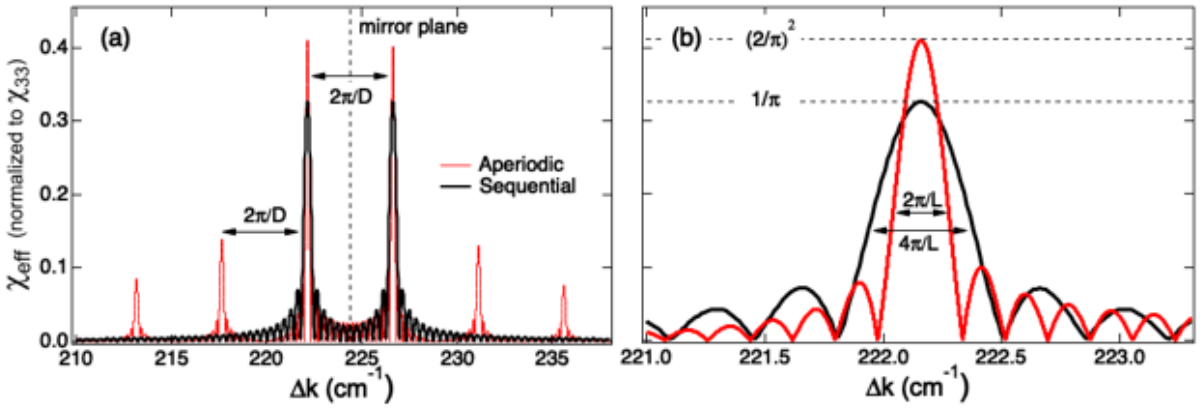

Figure 55. Effective nonlinearities of aperiodic and sequentially periodic structures. a) large scale that shows the secondary peaks of the aperiodic structure; b) close-up of one of the two main peaks. Values used in the simulation: Λ_1 = 28μm, D = 150μm, L = 35mm